TECHNOLOGICAL UNIVERSITY DELFT

DEPARTMENT OF AERONAUTICAL ENGINEERING

Report VTH-124

THEORETICAL AND EXPERIMENTAL INVESTIGATIONS OF INCOMPRESSIBLE LAMINAR BOUNDARY LAYERS WITH AND WITHOUT SUCTION

Ph.D THESIS

J.L. van INGEN

DELFT
the NETHERLANDS

OCTOBER, 1965

This PDF-file contains chapter 11:

Experimental investigation of a 15% thick laminar flow airfoil section with distributed suction

11. Experimental investigation of a 15°/o thick laminar flow airfoil section with distributed suction.

11.1. Introductory remarks.

In the present chapter some experimental work will be described which was performed on a NACA 64_2-A-215 airfoil section with boundary layer suction through a porous surface. The chord length of the model is 1.35 m; both the upper and the lower surface are porous between the 30°/o and 90°/o chord positions.

The model was tested in the low speed wind tunnel of the Department for Aeronautical Engineering at Delft. Measurements have been performed for angles of attack from -6 to +6 degrees and at Reynoldsnumbers R_c up till 8×10^6. The characteristics of the model without suction were determined by sealing the porous surface with a thin sheet of self-adhesive plastic.

The aims of the investigations were as follows:

a) To collect data on transition of two-dimensional boundary layers with suction. The results are to be used to check whether the method for predicting the transition point - proposed in chapter 9 - is applicable also for boundary layers with suction.

b) To obtain experimental data on the velocity distribution in a two-dimensional laminar boundary layer with suction including a separation point. These data are to be used for a comparison of boundary layer theory with experiment in the case of suction.

c) To collect some data on the amount of drag reduction obtained from laminarisation by means of suction.

Section 11.2 describes the experimental apparatus; the test methods and data reduction procedures are given in section 11.3 while results of the investigations are presented in sections 11.4 to 11.8.

In 11.4 the results of pressure distribution measurements are given. Section 11.5 describes the results of detailed boundary layer surveys on the upper surface of the model at $\alpha = 0^\circ$ and $R_c = 2.75 \times 10^6$. The results are presented both for the no-suction case and for one case with suction. The suction distribution for this case was chosen in such a way that laminar separation occurred in the suction region. Results of the

measurements are compared with boundary layer calculations using the momentum method and the multimoment method.
In section 11.6 some data on transition position and drag of the unsucked model are presented. Included are results of boundary layer calculations obtained from the momentum method together with calculated values of the amplification factor σ_a. Similar results for some cases with suction are discussed in section 11.7.
Finally, section 11.8 summarizes the results for the wake drag, suction drag and total drag for the configurations tested.

Since the experimental work has been very extensive no attempt will be made to describe it here in every detail. Only the main results will be quoted and especially those which are of significance for a comparison with laminar boundary layer theory and for the verification of the proposed method to compute the transition point.

11.2. Description of the experimental apparatus.

11.2.1. General.

The experiments were performed in the wind tunnel mentioned in section 10.2.1. The hot-wire equipment, described in section 10.2.3, was used again for the present investigation. In what follows some additional equipment will be described.

11.2.2. The model.

The airfoil section of the model is NACA 64_2-A-215 with a chord length of 1.35 m; coordinates of the airfoil section follow from table 11.1. The model was placed vertically between turntables in the ceiling and floor of the test section; the span obtained in this way being 1.25 m (see fig. 11.1).
The model is built up from two heavy steel spars connected by means of 10 ribs, in the suction region about 115 mm apart in the spanwise direction.

Suction is provided both for the upper and the lower surface between the $30^{o}/o$ and $90^{o}/o$ chord positions; the spanwise extent of the porous

surface is 0.805 m. Pressure orifices are present in one chord 344mm above the floor of the testsection (fig. 11.1); the positions of the orifices in chordwise direction follow from table 11.2. Two additional orifices (number 26 for the upper surface and number 25 for the lower surface) are placed in the midspan chord close to the trailing edge (see also table 11.2).

The inside of the model is divided into 40 different suction compartments, each with its own suction line, flow-regulating valve and -measuring device. A cross-section of the model is shown in fig. 11.2; the positions of the compartments in streamwise direction - measured along the contour of the model - have been given in table 11.3. In fig. 11.3 an enlargement of a part of fig. 11.2 is presented to show more clearly the construction of the porous surface. It consists of two layers of filtering paper supported by a metal screen which in turn rests on the ribs and between the ribs on wide-mesh paper honeycomb. Both the screen and the honeycomb have such a large open area that they provide a negligible resistance to the airflow and only act as support for the filtering paper.

Since at the position of the ribs the metal screen is supported directly on the ribs some obstruction to the suction flow is present here. However due to the fact that some leakage occurred between the two layers of filtering paper the inflow velocity at the position of the ribs was not so low as to cause important spanwise variations of the boundary layer characteristics. In typical cases transition to turbulent flow occurred on the ribs about 3 $^{o}/_{o}$ of the chordlength earlier than in sections midway between two ribs.

Some photographs of the model in various stages of construction are shown in figs 11.4-11.6. A schematic drawing of the suction compartments with the related suction equipment is shown in fig. 11.7.

The top surface of the compartments consists of 7 brass plates each containing 8 small metering holes (diameters ranging from 0.5 to 1 mm for different compartments). The 56 holes in each compartment have been drilled very accurately to the same diameter in order to obtain a constant inflow velocity over the span. The constancy is slightly impaired by local variations in porosity of the filtering paper

amounting to about 10 $^{o}/_{o}$. Since two layers of filtering paper have been used and since the major part of the resistance is provided by the metering holes, the actual variations in inflow velocity will have been far less than 10 $^{o}/_{o}$.

Figure 11.7 shows that the suction flow is measured at different stages. First of all the pressure drop is measured over the 8 metering holes in the plate covering the middle $^{1}/_{7}$th part of the span of a compartment. Then, from a calibration curve the suction flow into this middle section is known. The total flow into the compartment is measured by means of an orifice plate P_i and finally the flow into all 20 compartments in the upper or lower surface of the model is measured by means of a large orifice plate P_u or P_L (fig. 11.7). All these orifice plates have been calibrated individually before the tests.

Since the height of the compartments 19 and 20 in both the upper and lower surface is rather small it was not possible to provide them with plates containing metering holes.

The suction flow into individual compartments can be varied by means of the regulating valves V_i (fig. 11.7); the total flow from the model may be changed by means of a central valve V_c in the suction line to the pump.

For the experiments without suction the two layers of filtering paper were replaced by a large sheet of self-adhesive plastic.

From preliminary measurements of the pressure distribution on this model it was found that near the leading-edge an irregularity in the pressure distribution occurred which was related to an oscillation in the curvature of the model (fig. 11.8). Before starting the tests, described in the present work, the irregularity was removed to a great extent by smoothing the curvature of the model. This was accomplished by adding a thin plastic bump to the contour of the model. The largest thickness of this bump was 0.4 mm and occurred at $s/c = 0.05$ (see fig. 11.8).

11.2.3. Boundary layer traversing apparatus.

For the measurement of boundary layer velocity profiles the traversing gear, mentioned in section 10.2.3. was used. For some measurements

the hot-wire probe was replaced by a total head tube with a flattened opening (0.4 mm high).

11.2.4. Instruments for transition detection.

For transition detection two different devices have been employed. For measurements on the sealed model a small total head tube was used which could be moved in chordwise direction along the surface of the model by means of a small carriage. Transition from laminar to turbulent flow is indicated by this device through a sudden rise in total head.
For transition detection on the model with suction a "stethoscope" was used consisting of a total head tube connected to a microphone. Pressure fluctuations in the turbulent boundary layer could be made audible in this way. The device was mounted on a thin long pole which was handled by the observer to put the tube in contact with the model surface at different positions. In this way a quick estimate of the transition position could be obtained.

11.2.5. Other equipment.

For the measurement of wake drag a wake survey rake was used in combination with an "integrating manometer" (see for instance Pankhurst and Holder [111]).
For the pressure distribution measurements Betz-type manometers and inclined tubes have been used. The large number of pressures determining the suction distribution was measured on multiple type manometer banks. These pressures were recorded by photographing the manometers.

11.3. Test methods and reduction of data.

11.3.1. General.

Test methods and data reduction procedures have been - for so far possible - equal to those described in section 10.3. Some other methods will be described in the remainder of the present section.

11.3.2. The pressure distribution and "free stream speed".

The surface pressure distribution was measured in the same way as described in section 10.3.1. for the impervious model. The pressures were reduced to the velocity U at the edge of the boundary layer using equation (10.1). U was made non-dimensional with the "free stream speed" U_∞ defined by

$$\tfrac{1}{2}\rho U_\infty^2 = p_t - p_m \qquad (11.1)$$

with p_t indicating the total pressure of the pitot-static tube in the test-section (fig. 11.1). The free stream static pressure p_m is defined by

$$p_m = \frac{p_{w_+} + p_{w_-}}{2} \qquad (11.2)$$

where p_{w_+} and p_{w_-} are the static pressures, measured at two positions in the side walls of the testsection opposite the model. (fig. 11.1). It should be noted that this definition of the free stream static pressure differs from the one used in chapter 10.
The model is rather large compared with the dimensions of the testsection and therefore the remarks about tunnel wall influence on pressure distribution and free stream speed, made in section 10.3.1, apply also to the present case.

11.3.3. Determination of the suction distribution and suction drag coefficient.

The suction distribution. All orifice plates have been calibrated before the tests; the calibration curves were approximated by analytical expressions in order to simplify the subsequent data reduction procedure. The airflow into each compartment i was reduced to the suction flow coefficient c_{q_i} defined by

$$c_{q_i} = \frac{Q_i}{U_\infty b\, c} \qquad (11.3)$$

where Q_i = the total flow into compartment number i (m^3/sec)

U_∞ = free stream speed (m/sec)

b = span of porous surface (0.805 m)

c = airfoil chord (1.35 m).

Furthermore the total suction flow coefficients c_{q_u} and c_{q_ℓ} for the upper and the lower surfaces were found either from

$$c_{q_u} \text{ or } c_{q_\ell} = \frac{\sum_1^{20} Q_i}{U_\infty b\, c} = \sum_1^{20} c_{q_i} \qquad (11.4)$$

or from a direct measurement with orifice plate P_u or P_ℓ in figure 11.7. The mean suction velocity into each compartment follows from

$$\left(\frac{-v_o}{U_\infty}\right)_i = \frac{Q_i}{U_\infty b(\Delta s)_i} = \frac{c_{q_i}\, c}{(\Delta s)_i} \qquad (11.5)$$

in which $(\Delta s)_i$ denotes the width of the suction compartment given in table 11.3.

A typical suction distribution is shown in fig. 11.9; the measured points indicated in the figure are the mean suction velocities defined by equation (11.5). Within each compartment a slight variation of v_o may occur due the chordwise gradient of the surface pressure which gives rise to a chordwise variation of the pressure difference across the filtering paper. The resulting suction distribution is shown as a broken line in fig. 11.9. The actual inflow distribution will have been smoothed out due to leakage between the layers of filtering paper and between the paper and the metal screen. Hence for subsequent boundary layer calculations a continuous curve through the measured mean values was used as an approximation to the actual suction distribution.

The suction drag coefficient. In appendix 1 it is shown that the power required to induce the suction flow and to expell the air at free stream total head can be expressed in terms of a "suction drag coefficient" c_{d_s} defined by

$$c_{d_s} = c_p c_q \qquad (11.6)$$

In (11.6) c_p is given by

$$c_p = \frac{\Delta p}{\frac{1}{2}\rho U_\infty^2} \tag{11.7}$$

where Δp is the pressure rise, to be provided by the suction pump. In practical applications Δp will be the sum of the following pressure losses:

a. the loss in total head of the air in the boundary layer

b. the pressure drop through the porous surface

c. the pressure losses in the suction ducts inside the aircraft.

In what follows an ideal suction drag coefficient will be used including only the pressure drop mentioned under a. It will be assumed that the boundary layer air will have lost all its dynamic head before entering the porous surface.

For practical applications it certainly will be necessary to include the pressure drops b and c which will increase the suction drag. On the other hand the simple expression (11.6) will have to be replaced by a more accurate expression taking into account the difference in efficiency of the suction pump and the prime propulsion system of the aircraft (see appendix 1). This may lead to an appreciable reduction in suction drag and it may therefore be assumed that the ideal suction drag coefficient (11.6) gives a reasonable approximation of the suction drag to be expected in practice.

In analyzing the measurements a suction drag coefficient $c_{d_{s_i}}$ for each compartment was determined from

$$c_{d_{s_i}} = c_{p_i}\, c_{q_i} = \frac{\Delta p_i}{\frac{1}{2}\rho U_\infty^2}\, c_{q_i} \tag{11.8}$$

In (11.8) Δp_i is the difference between the free stream total head p_t and the surface static pressure p_i at the position of the i^{th} compartment. Hence

$$c_{p_i} = \frac{p_t - p_i}{\frac{1}{2}\rho U_\infty^2} = \bar{U}_i^2 \tag{11.9}$$

where $\bar{U}_i$ is the maximum value of $\bar{U}$ occurring at the outer surface of compartment number i.

The suction drag coefficient for the whole upper or lower surface of the model follows from a summation of $c_{d_{s_i}}$ for the 20 compartments related to that surface and hence

$$c_{d_{s_u}} \text{ or } c_{d_{s_\ell}} = \sum_{i=1}^{20} c_{d_{s_i}} \tag{11.10}$$

A mean pressure loss coefficient for each surface follows from

$$c_{p_u} \text{ or } c_{p_\ell} = \frac{\sum_{i=1}^{20} c_{p_i} c_{q_i}}{\sum_{i=1}^{20} c_{q_i}} \tag{11.11}$$

11.3.4. Determination of the wake drag.

From wake traverses. The drag of an airfoil without suction may be determined from the momentum loss in the wake; see for instance Pankhurst and Holder [111], Pfenniger [112] and Schlichting ([7], chapter 24). In appendix 1 the principle of this method is illustrated for a flat plate. It is also shown that the drag coefficient in the case of suction can not be found from the momentum loss in the wake only but that a "suction drag coefficient" has to be added.

The part of the drag determined from the momentum loss in the wake is called "wake drag". The wake drag is determined from the distribution of total head and static pressure through the wake which is measured by means of the wake survey rake. The results of the measurements have been converted to the wake drag coefficient using Pfennigers method [112].

Determination of the wake drag from the boundary layer velocity profile at the trailing-edge. Equation (A.5) in appendix 1 shows that the wake drag coefficient of one side of a flat plate at zero angle of attack follows from

$$c_{d_w} = \frac{2\,\theta_{t.e.}}{c} \qquad (11.12)$$

where $\theta_{t.e.}$ denotes the momentum loss thickness of the boundary layer at the trailing and c is the length of the plate. Of course the drag coefficient for both surfaces is found from (11.12) by adding the momentum loss thicknesses at the trailing-edge for both surfaces. Equation (11.12) also holds for an airfoil section if $\theta_{t.e.}$ is replaced by θ_∞ which is the momentum loss thickness of the wake at an infinite distance downstream of the trailing-edge. Due to the streamwise pressure gradient in the wake θ_∞ differs from $\theta_{t.e.}$. A relation between θ_∞ and $\theta_{t.e.}$ was derived by Squire and Young [11] using the momentum equation (2.15) and an empirical correlation between $\bar{U}$ and H in the wake. This leads to the following expression for the wake drag coefficient

$$c_{d_w} = 2\,\frac{\theta_{t.e.}}{c}\,(\bar{U}_{t.e.})^{\frac{H_{t.e.}+5}{2}} \qquad (11.13)$$

which reduces to (11.12) for the flat plate at zero angle of attack ($\bar{U}_{t.e.} = 1$). The derivation of (11.13) may be found for instance in Schlichting ([7], chapter 24).
The advantage of using (11.13) over the wake traverse method is that it may be applied to the upper and lower surface of the model separately so that changes in wake drag may easily be correlated with changes in transition position or suction intensity for either surface.

For the experiments without suction the boundary layer at the trailing edge was sufficiently thick to measure accurately the velocity profiles with a small rake of total head and static tubes fixed to the trailing-edge. For the experiments with suction the boundary layer thickness at the trailing-edge is greatly reduced (see fig. 11.17 for instance) and hence measurements with a rake are not sufficiently accurate. Therefore in all experiments with suction the velocity profiles at the trailing-edge have been measured with the flattened total head tube in combination with the traversing gear, described in section 11.2.3. No corrections for displacement effect of the tube have been applied. From

the measured velocity profiles δ^*, Θ and H were determined and substituted in (11.13) to find the wake drag coefficient.
The velocity profiles were not measured exactly at the trailing-edge but at the position of the most rearward pressure orifice. Since this orifice is placed at 98.5^o/o of the chord the wake drag coefficient found from equation (11.13) may be slightly too small.

A comparison of the wake drag found from equation (11.13) and from the wake survey method is shown in fig. 11.10 for some typical cases. In general a good correspondence is obtained.

11.4. Results of the pressure distribution measurements.

Results of the pressure distribution measurements for the no-suction case expressed in terms of $\bar{U}$ have been given in fig. 11.11 for different values of the angle of attack and a Reynoldsnumber based on chord of 5.5×10^6. Similar results have been obtained at other values of R_c ranging from 1×10^6 to 8.7×10^6. No systematic changes of $\bar{U}$ with R_c have been noted except for $R < 1.5 \times 10^6$. This change may be due to an appreciable thickening of the boundary layer at low speeds. Since in the subsequent experiments the main interest lies at the higher Reynoldsnumbers it will be assumed that the pressure distributions shown in fig. 11.11 can be used for boundary layer calculations at all values of the Reynoldsnumber R_c.
Some experiments with different amounts of suction were performed at $\alpha = 0^o$. No systematic influence of suction on the pressure distribution was found except near the trailing edge.
It may be noted that the suction velocities required to keep the boundary layer laminar are of the order of $10^{-4} U_\infty$ so that a direct influence of suction on the pressure distribution is difficult to imagine. An indirect effect of suction may have arisen as follows.
It was shown in chapter 10 that a discontinuity in the pressure gradient may occur where laminar separation is followed by turbulent reattachment. Since due to suction the positions of separation and transition may change, also the corresponding irregularities in the pressure distribution may change their positions. Since it was difficult

to install a large number of pressure orifices in the porous surface, the pressure distribution could not be determined very accurately and possible irregularities in the pressure distribution, referred to above, were not noticed. It has therefore been assumed that for all boundary layer calculations with and without suction the pressure distributions, shown in fig. 11.11, may be used.

11,5. Results of boundary layer surveys on the upper surface with and without suction.

Detailed surveys of the boundary layer in the midspan chord on the upper surface of the model were made at $\alpha = 0^o$ and $R_c = 2.75 \times 10^6$. For measurements in the laminar boundary layer with and without suction hot-wires have been used. Velocity profiles in the turbulent boundary layer, existing over the rear part of the surface in the no-suction case, have been measured with the flattened total head tube.
The results of the experiments will be discussed in the present section together with results of calculations using the momentum method of chapter 5 and the multimoment method of chapter 7.
Details of the pressure- and suction distributions used for the boundary layer calculations are shown in fig. 11.12 and table 11.4. For the calculations with the multimoment method λ_1 and λ_2 were approximated by polynomial expressions of the form

$$\lambda_1 \text{ or } \lambda_2 = \sum e_n \bar{x}^n \qquad (11.14)$$

The coefficients e_n have been listed in table 11.5. Results of the measurements and calculations are shown in figs 11.13 to 11.19.
Velocity profiles at some stations are shown in fig. 11.13; it follows that the laminar profiles with and without suction are reproduced reasonably well by the momentum method and the multimoment method. For the momentum method the correspondence is better than for the measurements discussed in chapter 10. It may be assumed that the better results in the present case stem from the fact that changes in $\frac{d\bar{U}}{d\bar{x}}$ are more gradual than for the impervious model.
The velocity profiles in the turbulent boundary layer without suction

are included in fig. 11.13. However, due to the large boundary layer thickness they could not be shown completely. Therefore, fig. 11.14 presents the velocity profiles in this region to a smaller scale. It is noticed that, as expected, a considerable reduction in boundary layer thickness and skin friction results from the application of suction.

Values of $\overline{\delta^*}$ and $\overline{\Theta}$ are shown in fig. 11.15 for the laminar boundary layers; a good correspondence between theory and experiment is shown. The experimentally determined values of the wall shear stress and the shape factor H for the laminar boundary layers with and without suction, are compared with the theoretical predictions in fig. 11.16. Again a good agreement is shown. It has to be remembered that the measured values of the wall shear stress were not obtained directly but resulted from the data reduction procedure, outlined in section 10.3.3.

According to the experiments laminar separation occurs at $\overline{x} = 0.56$ for the no-suction case and at $\overline{s} = 0.89$ in the case of suction. It may be seen that the momentum method predicts separation a bit early at $\overline{s} = 0.55$ and 0.88 respectively. As in earlier examples the multimoment method gives no clear indication of separation in the no-suction case. However, a short extrapolation of the calculated shear stress upstream of $\overline{s} = 0.50$ indicates separation at $\overline{s} = 0.55$. For the boundary layer with suction ($\lambda_2 \neq 0$) it follows from equation (7.63) that $a_2 \neq 0$ and hence equation (7.61) shows that $\frac{da_o}{d\overline{x}}$ may assume a non-zero value near separation. This is confirmed by fig. 11.17 from which it may be seen that the multimoment method predicts separation at $\overline{s} = 0.88$.

It is remarkable that in both cases with and without suction no difficulties were encountered in predicting the separation point. This situation is quite different from that for the boundary layer on the impervious model discussed in chapter 10. Possible explanations for this phenomenon are the following.

In the first place the better results may be due to the less accurate determination of the pressure distribution for the present case. This can best be explained by returning to fig.10.6 which shows the pressure

distribution in the separation region for the impervious model. If it should have been tried to determine this pressure distribution with a small number of orifices, then it is very likely that a mean curve would have been selected showing a more adverse pressure gradient upstream of separation than the actual curve. This may help the calculation method to predict separation.

Since in both cases with and without suction laminar separation was followed by transition further downstream it may be expected that the actual pressure distribution will appear like the one shown in fig. 10.5. With the available orifices this could not be observed however.

A second explanation, only applicable to the case with suction, is the following. The development of boundary layers with suction is not only determined by the pressure gradient but also by the suction velocity. Since the suction velocity is measured directly it can be determined much more accurately than the pressure gradient. Therefore it can be expected that the calculation of boundary layers with suction will be less sensitive to experimental error than boundary layers without suction.

In fig. 11.18 the results for δ^* and θ are replotted on a smaller scale to accomodate the experimental results for the turbulent boundary layer without suction. In this presentation δ^* and θ were not made non-dimensional to give an impression of the actual thicknesses involved. It is shown that a considerable reduction of the momentum loss thickness at the trailing-edge is obtained due to suction. According to equation (11.13) this implies a similar reduction in the wake drag coefficient. A further discussion of the drag reduction due to suction will be given in section 11.8.

In chapter 5 the characteristics of the momentum method have been discussed by means of the diagram in fig. 5.7. It was shown that known exact solutions, for which the momentum method supplies good results, are represented by the curves $P_3P_1P_4$, P_1P_2 and P_2P_4 in the diagram. It was therefore expected that the momentum method will give reasonably accurate solutions for those cases, which are represented in fig. 5.7 by a curve in the vicinity of $P_3P_1P_4$, P_1P_2 and/or P_2P_4. This is confirmed by the examples discussed in chapter 8 and 10 provided the cases with large discontinuities in pressure gradient or suction velocity are excluded.

Another curve can now be indicated in the vicinity of which the momentum method can be used with some confidence. It is the path traced out in the diagram by the boundary layer with suction discussed in the present section. This path is shown in fig. 11.19; numbers on the curve denote corresponding stations on the airfoil contour.

In view of the preceding remarks it seems justified to use the momentum method in those cases for which the corresponding curves in the M-Λ_1 plane are above or only a small distance below the curve in fig. 11.19. Since it was found that this requirement is fulfilled by most of the boundary layer flows encountered in the further analysis of the experiments with suction, it was decided only to use the momentum method for this analysis.

11.6. Transition and drag of the unsucked airfoil.

11.6.1. General.

The results of drag measurements with the wake survey rake are shown in fig. 11.20 for different values of the angle of attack as function of the Reynoldsnumber R_c.

A cross plot of fig. 11.20 is given in fig. 11.21; it shows the drag coefficient as function of α for different values of R_c. It can be seen that a "low-drag bucket" appears in the curves at low values of α and R_c. The drag rise at high values of $|\alpha|$ is caused by the fact that a pressure peak develops near the leading-edge which tends to move the transition forward. This is illustrated in fig. 11.22 where the results

of transition measurements for different values of R_c are shown. In sections 11.6.2 and 11.6.3 some more detailed results will be given for the upper surface of the model at $\alpha = 0$ and 3 degrees.

11.6.2. Transition and drag for the upper surface at $\alpha = 0^o$ without suction.

The transition position and wake drag coefficient for the upper surface of the model at $\alpha = 0^o$ are shown as function of the Reynoldsnumber R_c in fig. 11.23. It is seen that transition moves forward rather slowly with increasing values of R_c.

Calculations of the boundary layer characteristics including the amplification of unstable disturbances were made in the same way as described in section 9.8. Results are included in fig. 11.23 where curves are shown for constant values of the amplification factor $(\sigma_a)_{max}$ together with the calculated position of laminar separation (which is independent of the Reynoldsnumber). If, as in chapter 9, it is assumed that transition occurs for $(\sigma_a)_{max} = 9.2 - 11.2$ it follows that the method predicts the beginning of transition too early by an amount of about $6^o/o$ of the chord length at low values of R_c. This could be expected from the results shown for the EC 1440 airfoil in section 9.8.

It will be found in more examples that cases where transition occurs downstream or a short distance upstream from separation are predicted with less accuracy than those where transition occurs far upstream of separation. Possible explanations for this feature have been given already in section 9.8.

For the present case at higher values of R_c transition moves forward of the separation point (and of course separation is prevented then). At the highest value of R_c for which calculations have been made the distance between the calculated and the measured position of the beginning of transition is $2.5^o/o$ of the chord length.

11.6.3. Transition and drag for the upper surface at $\alpha = 3^o$ without suction.

In the present section detailed results will be presented for the upper surface at $\alpha = 3^o$. They will clearly illustrate the influence of changes

in the Reynoldsnumber R_c on transition position.
Fig. 11.24 shows results of boundary layer calculations using the momentum method; included is the critical Reynoldsnumber, according to Lin's formulae, which is independent of the Reynoldsnumber R_c. The values of $\frac{U\Theta}{\nu}$ depend on R_c according to the equation

$$\frac{U\Theta}{\nu} = \bar{U}.\bar{\Theta}.(R_c)^{\frac{1}{2}} \qquad (11.15)$$

obtained from the definitions of $\bar{U}$, $\bar{\Theta}$ and R_c. In equation (11.15) both $\bar{U}$ and $\bar{\Theta}$ are independent of R_c.
The results, shown in fig. 11.24, reveal an unstable region near the leading-edge caused by the adverse pressure gradient downstream of the peak in $\bar{U}$ at $\bar{s} = 0.04$ (see fig. 11.11). At $R_c = 1.94 \times 10^6$ for instance, the boundary layer becomes first unstable at $\bar{s} = 0.047$, then becomes stable again at $\bar{s} = 0.129$ and definitely unstable at $\bar{s} = 0.189$. Whether or not the unstable region may provoke transition near the leading-edge will depend on the value of the Reynoldsnumber R_c. It can be expected that only at high values of R_c the amplification rate will be high enough for this. This is confirmed by the results of further calculations described below.
The values of the amplification factor σ_a are shown in fig. 11.25a and b for several frequencies at two different values of R_c. The envelope of the curves for different frequencies gives the maximum amplification factor $(\sigma_a)_{max}$. Similar calculations have been made for other values of R_c, the resulting envelopes have been collected in fig. 11.26. It can be seen from this figure that for high values of R_c the amplification factor reaches the critical value 9.2 very close to the leading-edge and hence transition can be expected to occur very early. This is confirmed by the experimental results shown in fig. 11.27. Included in the figure are the calculated positions of separation and curves for constant values of $(\sigma_a)_{max}$. Again it is shown that, when transition is preceded by laminar separation, the distance between the measured and predicted position of transition is of the order of $10^o/o$ of the chord. For increasing R_c however, transition moves forward of the calculated laminar separation point and the predicted separation position becomes

more accurate. Even the rather sudden shift forward at $R_c > 6 \times 10^6$ is predicted with reasonable accuracy.

11.7. Transition and drag with suction at $\alpha = 0^o$.

11.7.1. General.

In the present section (11.7) some data will be presented on transition position, wake drag, ideal suction drag and total drag for 7 series of measurements at $\alpha = 0$ with suction. Results of boundary layer calculations will be presented and the measured transition positions will be compared with results of amplification calculations. Some specific details of the 7 series have been given in table 11.6.
For series 1, to be described in section 11.7.2, the flow regulating valves V_i (see fig. 11.7) have been set in such a way that the resulting suction distribution - according to a very rough calculation - would be sufficient to prevent transition. Then the setting of the central valve (V_c in fig. 11.7) was changed to collect data at different values of c_q for the same type of suction distribution.
In series 2 (section 11.7.3) all valves V_i were left open and hence the suction distribution was determined by the built-in resistances of orifice plates and suction ducts. Again the total amount of flow was changed by means of the central valve V_c.
For series 3 (section 11.7.4) the valves have been set in such a way that the pressure underneath the filtering paper was the same for all compartments in the upper surface. Hence a continuous suction distribution was obtained. The constant pressure was given such a value that transition occurred at the end of the porous surface.
In the experiments, mentioned above, it was found to be impossible to keep the boundary layer laminar at values of R_c above 3.5×10^6. At higher speeds the inherent surface roughness of the filtering paper became supercritical causing transition due to roughness. Therefore, in some further experiments, the filtering paper was covered by a sheet

of tightly stretched fine mesh nylon (see fig. 11.6). In this way it became possible to keep the boundary layer laminar up till $R_c = 6.5 \times 10^6$. Some measurements on the upper surface, with the nylon present, have been described as series 4,5,6 and 7 in section 11.7.5. For these series the valves V_i were set by trial and error in such a way that transition occurred at the end of the porous surface with the smallest possible amount of suction. Once this was achieved the total amount of flow was changed by means of the central valve.
Finally in section 11.7.6 a comparison will be given between the calculated and measured transition positions for series 1-7.

11.7.2. Transition and drag with suction; series 1.

Values of the wake drag, ideal suction drag and total drag for the upper and lower surfaces combined are shown in fig. 11.28. The wake drag decreases and the suction drag increases with increasing values of c_q. The total drag shows a minimum value at $c_q = 7.5 \times 10^{-4}$; this corresponds to the situation when transition occurs close to the trailing-edge. This is shown clearly in figs 11.29 and 11.30, where the drag has been given for the upper and lower surface separately and a comparison is made with the measured transition position.
The suction velocity distribution for the upper surface is shown in fig. 11.31 for some values of c_{q_u}. Included as a dotted line is the suction distribution required at this value of R_c to keep the boundary layer neutrally stable downstream of the beginning of the porous region ($\bar{s} = 0.32$). This suction distribution is easily found from the momentum method and Lin's formulae (section 9.4) if the requirement is made that $\frac{U\Theta}{\nu}$ and $(\frac{U\Theta}{\nu})_{crit}$ are equal.
Fig. 11.31 shows that in the beginning the suction velocity at all values of c_{q_u} is much higher than required for stabilisation. Further downstream the suction intensity is less than required for stabilisation.
Results of boundary layer calculations using the experimentally determined suction distributions for different values of c_{q_u} are plotted in the M-Λ_1 plane shown in fig. 11.32. It is seen that in all cases the path traced out in the diagram ends up on the left-hand-side

boundary. This implies that eventually the laminar boundary layer separates from the surface unless transition occurs earlier. Indicated in the figure are the values of M and Λ_1 corresponding to the measured transition positions. It follows that only for $c_{q_u} = 0$ and for very high values of c_{q_u} separation is actually reached. For intermediate suction quantities laminar separation is prevented by transition. Values of $^{10}\log \frac{U\theta}{\nu}$ and $^{10}\log (\frac{U\theta}{\nu})_{crit}$ are shown in fig. 11.33 for different values of c_{q_u}. It can be seen that for $c_{q_u} = 0$ the boundary layer becomes unstable at $\bar{s} = 0.33$ coinciding almost with the beginning of the porous surface. For the non-zero values of c_{q_u} the suction in the first part of the porous region is so intense that a strong stabilising influence occurs. ($^{10}\log (\frac{U\theta}{\nu})_{crit} >> {}^{10}\log \frac{U\theta}{\nu}$). However, downstream of the pressure minimum at $\bar{s} = 0.42$ (see fig. 11.31) the adverse pressure gradient rapidly compensates the effect of suction and the boundary layer becomes unstable. Only at very high values of c_{q_u} would the boundary layer remain stable as far as the trailing-edge.

An interesting feature follows from a comparison of fig. 11.31 and 11.33. It is noticed that the boundary layer becomes unstable very close to the position where $|v_o|$ falls below the value needed to obtain a neutrally stable boundary layer over the full length of the porous surface. This implies that boundary layer stability - at least according to the momentum method - has a very poor memory for its upstream history. This may be explained by observing that the influence of suction on stability lies principally in the change of the critical Reynoldsnumber while the changes in $\frac{U\theta}{\nu}$ are much less. (fig. 11.33). Since $\frac{U\theta}{\nu}$ depends on the history of the boundary layer but the shape of the velocity profile - and hence $(\frac{U\theta}{\nu})_{crit}$ - is primarily determined by the local pressure gradient and suction velocity, it is clear that the upstream history is of secondary importance only. Therefore it is clearly not economic to apply suction to early; the most economic suction distribution will be obtained by carefully tailoring the suction velocity distribution to the local needs of the boundary layer.

Using $\frac{U\theta}{\nu}$ and $(\frac{U\theta}{\nu})_{crit}$ from fig. 11.33 for different values of c_{q_u} amplification calculations have been made for different frequencies. The resulting envelopes, denoting the maximum amplification factor, are shown in fig. 11.34. It follows that only for $c_{q_u} < 3.39 \times 10^{-4}$ the critical value 9.2 is reached in the porous region. This implies that transition can only be expected to occur in the suction region for $c_{q_u} < 3.39 \times 10^{-4}$. In figure 11.35 the measured transition region is compared with the calculated positions for which $(\sigma_a)_{max} = 9.2$ and 11.2. Although the calculated positions are a little further downstream than the measured transition position, a satisfactory prediction of the transition region will be obtained for $c_{q_u} < 3.5 \times 10^{-4}$ if it is assumed that transition occurs as soon as $(\sigma_a)_{max}$ reaches the values 9.2-11.2. At higher values of c_{q_u} transition is caused by a preceding separation in which case the proposed method for the prediction of transition can not be expected to provide accurate results. This is confirmed by the results shown in fig. 11.35.

11.7.3. Transition and drag with suction; series 2.

For this series the same measurements and calculations have been performed as for series 1; results are presented in figs 11.36 - 11.39.

11.7.4. Transition and drag with suction; series 3.

This case is included since it shows one of the examples for which the distance between the measured and calculated transition positions is rather large. Final results are shown in fig. 11.40; it follows that transition is preceded by laminar separation for all values of c_{q_u} explaining the unsatisfactory agreement between theory and experiment.

11.7.5. Transition and drag with suction: series 4-7: $\alpha = 0^{\circ}$ upper surface only; filtering paper covered with nylon.

For series 4-7 the filtering paper was covered with a sheet of fine mesh nylon. In the present section some results of measurements and calculations for the upper surface will be presented. For series 4-7

the valve settings were found by trial and error. It was attempted to obtain, with the minimum amount of suction, a boundary layer for which transition occurred at the end of the porous surface.

The suction distributions obtained in this way for different values of R_c are shown in fig. 11.41. Also shown for two values of R_c is the v_o-distribution required to keep the boundary layer neutrally stable throughout the suction region. It can be seen that in all cases too much suction has been applied in the forward part of the porous region. This may be explained as follows. If the suction velocities are chosen very low it is possible that - inadvertently - local outflow occurs giving rise to premature transition. Apparently the suction velocities used in the experiments were chosen on the safe side.

Near the trailing-edge the suction intensity is in general less than that needed for stabilisation.

Boundary layer calculations, using the momentum method, have been made for the experimentally determined suction distributions shown in fig. 11.41. Results of the calculations have been plotted in the M-Λ_1 diagram (fig. 11.42) where also the measured transition position is indicated. It follows that in all cases transition near the end of the porous surface is caused by laminar separation. It is interesting to note that for $R_c = 3.37 \times 10^6$ the boundary layer nearly separates at $\bar{s} = 0.68$ but downstream of this point the suction intensity is increased which postpones separation to a position further downstream.

Measurements at other values of c_{q_u} have been made for all values of R_c by changing the setting of the central valve V_c (see fig. 11.7). At the lower values of c_{q_u} transition may be preceded by laminar separation. This is shown in figs 11.43 - 11.46 where results of transition measurements have been compared with calculated positions. It can be seen that transition is predicted within 5 or $10^o/o$ chord accurately except when transition is preceded by separation. Especially at $R_c = 3.37 \times 10^6$ large discrepancies between theory and experiment occur (fig. 11.43). However, fig. 11.42 shows that in this case for the suction distribution obtained by trial and error the boundary layer is on the verge of separation over a long distance and hence an inaccurate result may be expected.

A similar remark applies for other values of c_{q_u} at $R_c = 3.37 \times 10^6$. Finally figures 11.47 - 11.50 show the drag coefficients and transition positions as function of c_{q_u} for series 4 to 7. There is a good correlation between drag and transition position. This is shown more clearly in fig. 11.51 where the total drag coefficient for the upper surface is plotted as a function of the position where transition starts. It is noticed that the minimum value of the total drag coefficient is obtained when transition occurs near the end of the porous region.

1.7.6. Summary of the comparisons between the measured and calculated transition positions.

Fig. 11.52 has been prepared to summarize all results obtained in the preceding comparisons of the measured and predicted transition positions. The figure shows the position where $(\sigma_a)_{max}$ reaches the critical value 9.2 as function of the beginning of the experimentally determined transition region. Where transition is preceded by laminar separation a full symbol has been used. Data are shown for all values of c_q for which in the preceding figures a measured transition region has been indicated by the symbol ⊢——⊣ . Experiments in which transition occurred downstream of the porous region have been omitted.

It may be concluded from the figure that the beginning of transition is predicted within $\pm$ 10°/o of the chord length when transition is not preceded by laminar separation. Where separation is the cause of transition the distance between the predicted and actual beginning of transition may become larger.

It should be remembered that in most of the experiments with suction transition moves downstream very rapidly with increasing c_q. For these cases a satisfactory agreement between theory and experiment may have been obtained although fig. 11.52 shows a large distance between the measured and predicted transition positions. Of course a better correlation will be shown for these cases if a comparison is made between the theoretically and the experimentally determined value of c_q which is required to bring transition back to a certain position.

11.8. Summary of the drag coefficients obtained with and without suction.

In the preceding section some results of drag measurements at $\alpha = 0^{o}$ with suction have been presented. It was found that the minimum total drag is obtained when transition occurs near the end of the porous surface. In the present section results will be presented for an extended series of measurements including values of $\alpha \neq 0$. The presentation will be confined to those values of c_q for which transition occurred at the end of the porous surface. It may be assumed that these situations correspond to the condition with minimum total drag at the given value of α and R_c.
Fig. 11.53a and b show the results for the upper surface covered with nylon (series 4-7) both in the familiar logarithmic presentation and to a linear scale. A comparison is made with the drag of a flat plate with constant suction velocity $\frac{-v_o}{U} = 1.18 \times 10^{-4}$ discussed in section 9.8.1. It may be seen that the drag of the airfoil decreases with increasing R_c in the same way as for the flat plate. An appreciable drag reduction due to suction is obtained; the amount of the reduction is plotted vs R_c in fig. 11.54. At the highest value of R_c for which measurements have been made (6.16×10^{6}) the reduction in total drag is $63^{o}/o$.
Although a comparison with the flat plate results is not entirely justified due to the difference in pressure distribution, it may be seen that the drag reduction with increasing R_c shows the same trend for the airfoil as for the flat plate. Extrapolating the results of the experiments to full scale values of R_c ($\approx 25 \times 10^{6}$) shows that the drag reduction obtained may be of the order of $75^{o}/o$. This agrees with results obtained in different experiments mentioned in chapter 1.
Results for the upper and lower surface combined, for the experiments without the nylon covering, are shown in fig. 11.55 for different values of $R_c \leqslant 3.37 \times 10^{6}$. Included in the figure is the drag of the model with the sealed porous surface. It may be seen that drag reductions of the order of $50^{o}/o$ are obtained at these low values of R_c.

11.9. Concluding remarks on the experiments with suction.

From the results discussed in the present chapter it follows that both the momentum method and the multimoment method provide a good agreement

Table 11.1: Coordinates of suction model(NACA 64_2-A-215)

x_p mm	y_p upper mm	y_p lower mm
0	0.13	0
10	23.91	16.80
20	29.57	23.42
50	45.62	36.06
75	55.50	43.32
100	63.63	49.28
150	77.01	58.81
200	87.94	66.16
250	96.65	71.97
300	103.59	76.48
350	109.13	79.91
400	113.40	82.38
450	116.40	83.84
500	118.06	84.28
550	118.24	83.59
600	116.77	81.44
650	113.97	78.21
700	110.03	74.12
750	105.13	69.30
800	99.27	63.928
850	92.68	
900	85.34	straight between x_p = 817.5; y_p = 61.93 and x_p = 1350; y_p = 0.43
950	77.36	
1000	68.89	
1050	60.02	
1100	50.68	
1150	40.80	
1200	30.82	
1250	20.75	
1300	10.56	
1350	0.43	0.43

Table 11.2: Position of pressure orifices in impervious model.

no	upper surface $\bar{x}$ %	upper surface $\bar{s}$ %	lower surface $\bar{x}$ %	lower surface $\bar{s}$ %
0	0	0	0	0
1	0.49	1.45	0.50	1.21
2	1.02	2.16	1.01	1.89
3	1.42	2.69	1.16	2.07
4	2.03	3.40	2.00	3.03
5	2.50	3.94	2.47	3.56
6	3.01	4.50	2.98	4.09
7	4.04	5.63	4.00	5.17
8	5.03	6.70	5.01	6.22
9	6.36	8.10	5.22	6.44
10	7.11	8.81	7.02	8.30
11	7.52	9.33	7.50	8.87
12	10.04	11.93	9.94	11.33
13	15.02	17.06	13.20	14.61
14	15.16	17.19	14.97	16.39
15	20.01	22.14	19.99	21.45
16	29.92	32.12	29.93	31.39
17	39.95	42.16	39.97	41.44
18	49.99	52.23	50.05	51.56
19	60.02	62.31	60.06	61.63
20	65.00	67.33	70.02	71.68
21	70.01	72.39	73.28	74.96
22	78.18	80.82	80.01	81.72
23	80.02	82.70	86.64	88.40
24	89.40	92.28	89.82	91.59
25	90.03	92.92	98.55	100.34
26	98.54	101.58	–	
tr.edge	100.00	103.07	100.00	101.81

Table 11.3: Dimensions of suction compartments

no	upper surface $\bar{s}$ beginning	upper surface $\bar{s}$ mean	upper surface $\bar{s}$ end	upper surface $\Delta\bar{s}$	lower surface $\bar{s}$ beginning	lower surface $\bar{s}$ mean	lower surface $\bar{s}$ end	lower surface $\Delta\bar{s}$
1	0.3210	0.3362	0.3513	0.0303	0.3151	0.3299	0.3446	0.0295
2	0.3513	0.3662	0.3811	0.0298	0.3446	0.3597	0.3748	0.0302
3	0.3811	0.3960	0.4109	0.0298	0.3748	0.3895	0.4041	0.0293
4	0.4109	0.4257	0.4405	0.0296	0.4041	0.4189	0.4336	0.0295
5	0.4405	0.4555	0.4705	0.0300	0.4336	0.4480	0.4624	0.0288
6	0.4705	0.4854	0.5003	0.0298	0.4624	0.4775	0.4925	0.0301
7	0.5003	0.5150	0.5297	0.0294	0.4925	0.5074	0.5222	0.0297
8	0.5297	0.5448	0.5598	0.0301	0.5222	0.5373	0.5523	0.0301
9	0.5598	0.5746	0.5893	0.0295	0.5523	0.5671	0.5818	0.0295
10	0.5893	0.6044	0.6195	0.0302	0.5818	0.5970	0.6122	0.0304
11	0.6195	0.6343	0.6490	0.0295	0.6122	0.6270	0.6417	0.0295
12	0.6490	0.6644	0.6798	0.0308	0.6417	0.6570	0.6723	0.0306
13	0.6798	0.6946	0.7094	0.0296	0.6723	0.6871	0.7018	0.0295
14	0.7094	0.7247	0.7399	0.0305	0.7018	0.7170	0.7321	0.0303
15	0.7399	0.7546	0.7692	0.0293	0.7321	0.7467	0.7613	0.0292
16	0.7692	0.7845	0.7998	0.0306	0.7613	0.7764	0.7915	0.0302
17	0.7998	0.8141	0.8283	0.0285	0.7915	0.8053	0.8190	0.0275
18	0.8283	0.8463	0.8643	0.0360	0.8190	0.8370	0.8550	0.0360
19	0.8643	0.8837	0.9030	0.0387	0.8550	0.8737	0.8924	0.0374
20	0.9030	0.9217	0.9404	0.0374	0.8924	0.9110	0.9295	0.0371

Table 11.4: Details of the pressure- and suction distributions used in the boundary layer calculations of section 11.5.

$\bar{s}$	$\bar{U}$	$\frac{d\bar{U}}{d\bar{x}}$	λ_1	λ_2	$\frac{-V_o}{U_\infty} 10^4$
0	0.110000	66.48276	0.95480		
0.01	0.61520	34.20576	0.62836		
0.02	0.82390	14.54562	0.37600		
0.03	0.93920	7.53191	0.25104		
0.04	0.99240	4.06891	0.16935		
0.05	1.02470	2.57748	0.12903		
0.06	1.04767	1.93405	0.11316		
0.07	1.06526	1.56981	0.10507		
0.08	1.07944	1.28452	0.09675		
0.09	1.09133	1.07352	0.08981		
0.10	1.10127	0.93110	0.08565		
0.11	1.11031	0.83970	0.08417		
0.12	1.11840	0.77081	0.08360		
0.13	1.12582	0.71542	0.08344		
0.14	1.13271	0.66286	0.08269		
0.15	1.13907	0.60924	0.08092		
0.16	1.14492	0.56052	0.07897		
0.17	1.15031	0.51390	0.07653		
0.18	1.15528	0.47010	0.07377		
0.19	1.15980	0.42976	0.07088		
0.20	1.16391	0.39348	0.06805		
0.21	1.16770	0.36357	0.06579		
0.22	1.17119	0.33529	0.06335		
0.23	1.17442	0.30938	0.06093		
0.24	1.17738	0.28395	0.05819		
0.25	1.18010	0.26091	0.05556		
0.26	1.18262	0.24333	0.05376		
0.27	1.18498	0.22948	0.05254		
0.28	1.18721	0.21576	0.05112		
0.29	1.18930	0.20472	0.05014		
0.30	1.19130	0.19514	0.04936		
0.31	1.19320	0.18500	0.04826		
0.32	1.19500	0.17500	0.04705	0.06405	0.745
0.33	1.19670	0.16500	0.04568	0.10513	1.205
0.34	1.19830	0.15500	0.04415	0.15061	1.702
0.35	1.19980	0.14600	0.04275	0.19567	2.181
0.36	1.20121	0.13514	0.04065	0.23643	2.600
0.37	1.20249	0.12000	0.03705	0.27409	2.975
0.38	1.20360	0.10129	0.03209	0.30983	3.320
0.39	1.20451	0.08124	0.02639	0.34398	3.640
0.40	1.20520	0.05581	0.01858	0.37838	3.955
0.41	1.20560	0.02195	0.00749	0.41275	4.262
0.42	1.20560	-0.02391	-0.00835	0.44713	4.562
0.43	1.20508	-0.07981	-0.02856	0.48157	4.855
0.44	1.20401	-0.13481	-0.04941	0.51554	5.135
0.45	1.20239	-0.18552	-0.06963	0.54914	5.406
0.46	1.20031	-0.23052	-0.08859	0.58259	5.668
0.47	1.19779	-0.27052	-0.10644	0.61486	5.910
0.48	1.19491	-0.30552	-0.12306	0.64820	6.160
0.49	1.19169	-0.33567	-0.13839	0.67978	~~6.202~~ 6.400
0.50	1.18821	-0.36024	-0.15198	0.71509	6.640
0.51	1.18450	-0.38190	-0.16485	0.74819	6.850
0.52	1.18060	-0.40230	-0.17764	0.78444	7.120

Table 11.4: Continued; Details of the pressure- and suction distributions used in the boundary layer calculations of section 11.5.

$\bar{s}$	$\bar{U}$	$\frac{d\bar{U}}{d\bar{x}}$	λ_1	λ_2	$\frac{-V_o}{U_\infty} 10^4$
0.53	1.17650	-0.42114	-0.19018	0.81911	7.357
0.54	1.17219	-0.43986	-0.20312	0.85402	7.580
0.55	1.16772	-0.45576	-0.21517	0.88859	7.800
0.56	1.16308	-0.47076	-0.22719	0.92351	8.018
0.57	1.15831	-0.48486	-0.23914	0.95620	8.212
0.58	1.15340	-0.49614	-0.25005	0.98520	8.370
0.59	1.14840	-0.50620	-0.26064	1.00793	8.472
0.60	1.14330	-0.51529	-0.27100	1.02565	8.530
0.61	1.13809	-0.52120	-0.27995	1.03712	8.535
0.62	1.13281	-0.53010	-0.29074	1.04493	8.510
0.63	1.12751	-0.53460	-0.29932	1.05057	8.468
0.64	1.12191	-0.53930	-0.30827	1.05623	8.426
0.65	1.11679	-0.54310	-0.31673	1.06041	8.375
0.66	1.11131	-0.54640	-0.32514	1.06411	8.320
0.67	1.10580	-0.54980	-0.33377	1.06602	8.252
0.68	1.10030	-0.55330	-0.34260	1.06694	8.178
0.69	1.09481	-0.55670	-0.35152	1.06691	8.098
0.70	1.08929	-0.56050	-0.36086	1.06534	8.008
0.71	1.08369	-0.56520	-0.37098	1.06252	7.910
0.72	1.07802	-0.56990	-0.38132	1.05865	7.805
0.73	1.07228	-0.57452	-0.39183	1.05430	7.700
0.74	1.06652	-0.58010	-0.40321	1.05111	7.605
0.75	1.06069	-0.58614	-0.41517	1.04776	7.508
0.76	1.05479	-0.59080	-0.42641	1.04446	7.415
0.77	1.04881	-0.59580	-0.43816	1.04220	7.330
0.78	1.04281	-0.60030	-0.44976	1.03975	7.245
0.79	1.03678	-0.60238	-0.45975	1.03813	7.167
0.80	1.03072	-0.60924	-0.47363	1.03676	7.092
0.81	1.02459	-0.61414	-0.48630	1.03630	7.024
0.82	1.01841	-0.62371	-0.50299	1.03302	6.938
0.83	1.01209	-0.63886	-0.52474	1.03531	6.890
0.84	1.00561	-0.65886	-0.55121	1.03577	6.830
0.85	0.99889	-0.68371	-0.58270	1.03745	6.778
0.86	0.99191	-0.71414	-0.62011	1.03978	6.730
0.87	0.98458	-0.75024	-0.66395	1.04266	6.685
0.88	0.97691	-0.78438	-0.70761	1.04645	6.645
0.89	0.96890	-0.81529	-0.74999	1.05114	6.610
0.90	0.96060	-0.84486	-0.79270	1.05595	6.575
0.91	0.95200	-0.87600	-0.83855	1.06247	6.543
0.92	0.94309	-0.90514	-0.88423	1.06778	6.516
0.93	0.93391	-0.92910	-0.92651	1.07322	6.482
0.94	0.92450	-0.95100	-0.96828	1.07993	6.455
0.95	0.91490	-0.97260	-1.01130	1.08710	6.430
0.96	0.90510	-0.99230	-1.05391	1.09357	6.400
0.97	0.89510	-1.01100	-1.09707	1.10019	6.370
0.98	0.88490	-1.02750	-1.13945	1.10696	6.340
0.99	0.87451	-1.04120	-1.18025	1.11388	6.310
1.00	0.86400	-1.05600	-1.22381	1.12091	6.280
1.01	0.85340	-1.06500	-1.26205	1.12805	6.250
1.02	0.84270	-1.07500	-1.30284	1.13549	6.221
1.03	0.83190	-1.08500	-1.34506	1.14363	6.195
1.04	0.82100	-1.09500	-1.38882	1.15115	6.165

Table 11.5: Coefficients e_n in eq. (11.14) for the suction model (0.123 + 4 denotes $0.123 \times 10^{+4}$)

$\bar{x} = \bar{s} + 0.0013$

	e_n for λ_1			
n	$0.0413 \leqslant \bar{x} < 0.3213$	$0.3213 \leqslant \bar{x} < 0.6013$	$0.6013 \leqslant \bar{x} < 0.8313$	$0.8313 \leqslant \bar{x} < 1.0413$
0	+0.487766 + 0	+0.1662923 + 2	-036908471 + 1	+0.22592310 + 3
1	-0.134523 + 2	-0.1986979 +3	+0.23718205 + 2	-0.10055939 + 4
2	+0.181436 + 3	+0.9103331 + 3	-0.45759292 + 2	+0.14528307 + 4
3	-0.125194 + 4	-0.1938422 + 4	-0.58434123 + 1	-0.24580937 + 3
4	+0.463313 + 4	+0.1738382 + 4	+0.11366534 + 3	-0.13063590 + 4
5	-0.880172 + 4	-0.1237675 + 3	-0.12648480 + 3	+0.12080765 + 4
6	+0.676231	-0.4795547 + 3	+0.43524752 + 2	-0.33028708 + 3

	e_n for λ_2		
n	$0.3213 \leqslant \bar{x} < 0.6013$	$0.6013 \leqslant \bar{x} < 0.8313$	$0.8313 \leqslant \bar{x} < 1.0413$
0	+0.29218010 + 1	-0.10669276 + 2	-0.36265370 + 2
1	-0.53116491 + 2	+0.41452406 + 2	+0.17009344 + 3
2	+0.28212314 + 3	-0.32546333 + 2	-0.24884816 + 3
3	-0.59331533 + 3	-0.19311793 + 2	+0.40613195 + 2
4	+0.37822004 + 3	+0.22741090 + 1	+0.22746742 + 3
5	+0.34827455 + 3	+0.47776766 + 2	-0.20825789 + 3
6	-0.41868191 + 3	-0.27946329 + 2	+0056318055 + 2

Table 11.6: Some specific details of 7 series of measurements with suction.

series	α	$R_c \times 10^{-6}$	porous surface	valve settings V_i
1	0	3.37	filtering paper	for roughly calculated stability
2	0	3.37	"	open
3	0	2.75	"	continuous V_o
4	0	3.37	paper + nylon	trial and error
5	0	4.50	"	"
6	0	5.50	"	"
7	0	6.16	"	"

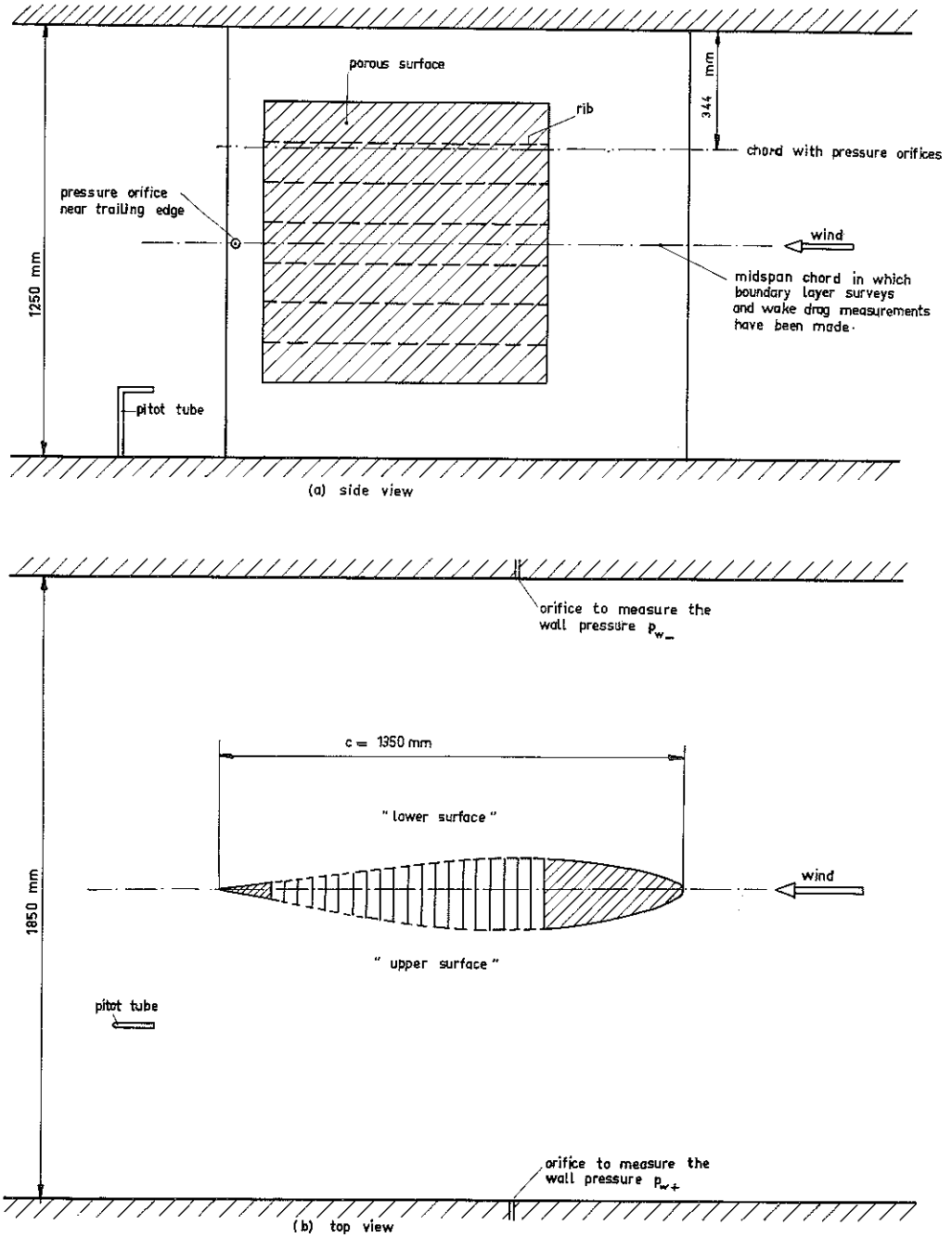

FIG. 11.1: SET UP OF SUCTION MODEL IN WINDTUNNEL

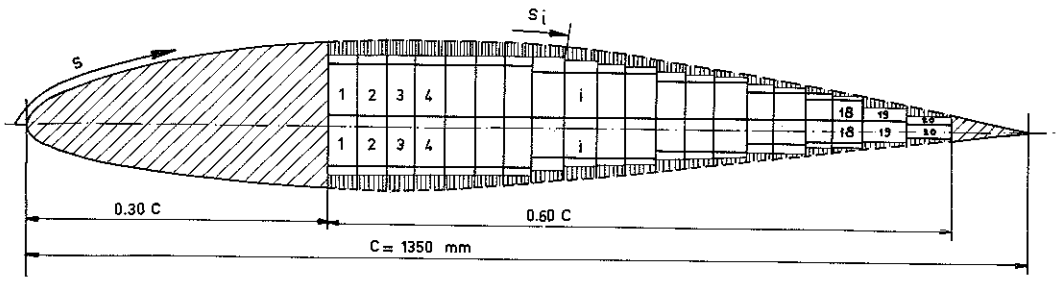

FIG. 11.2: CROSS SECTION OF MODEL SHOWING SUCTION COMPARTMENTS

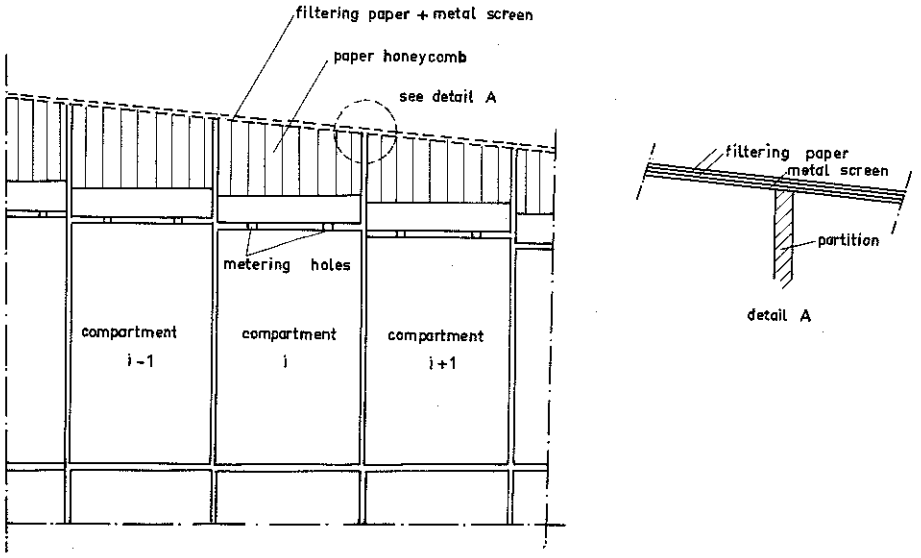

FIG. 11.3 : CONSTRUCTION OF THE POROUS SURFACE

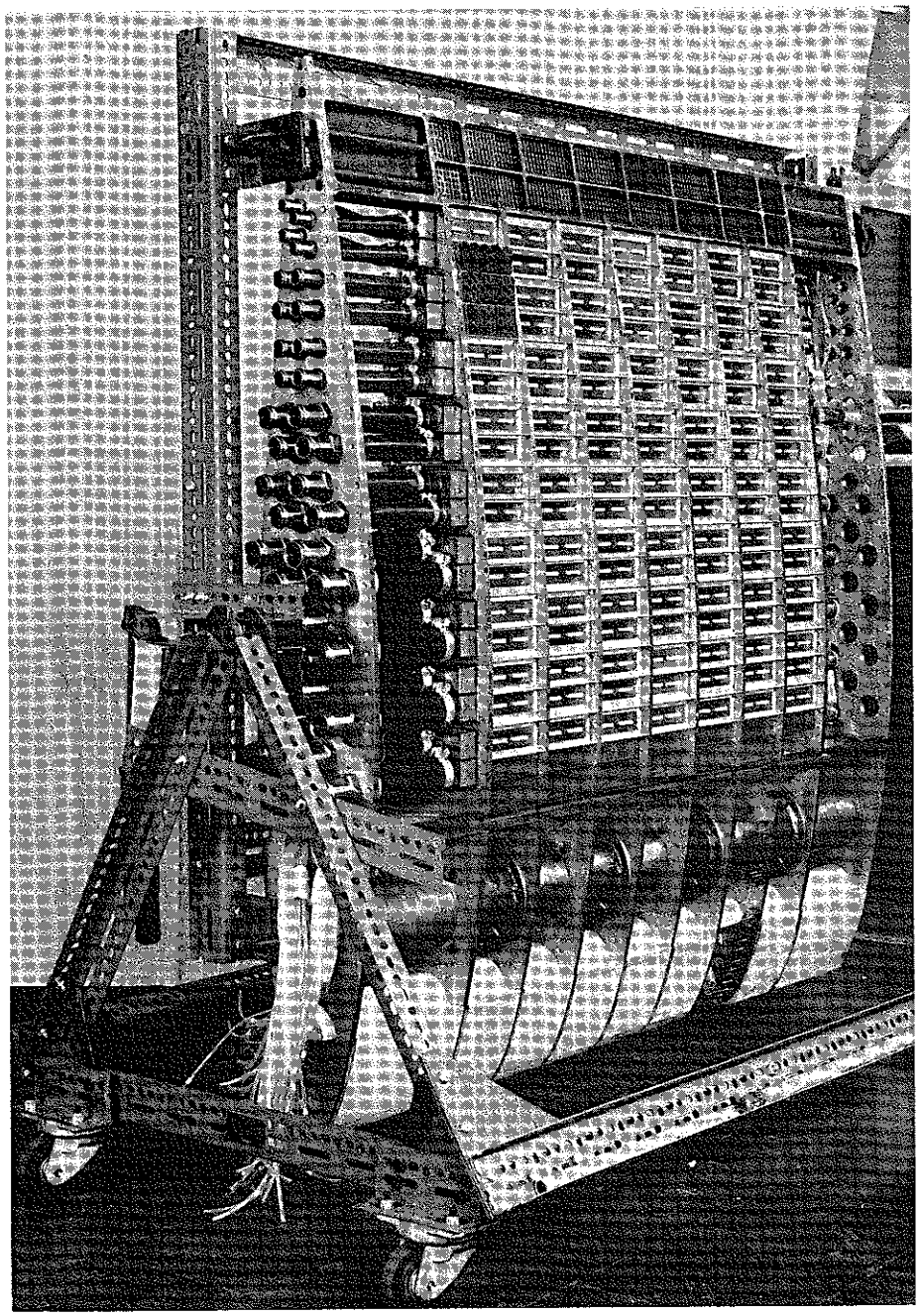

FIG. 11.4: INTERIOR OF MODEL

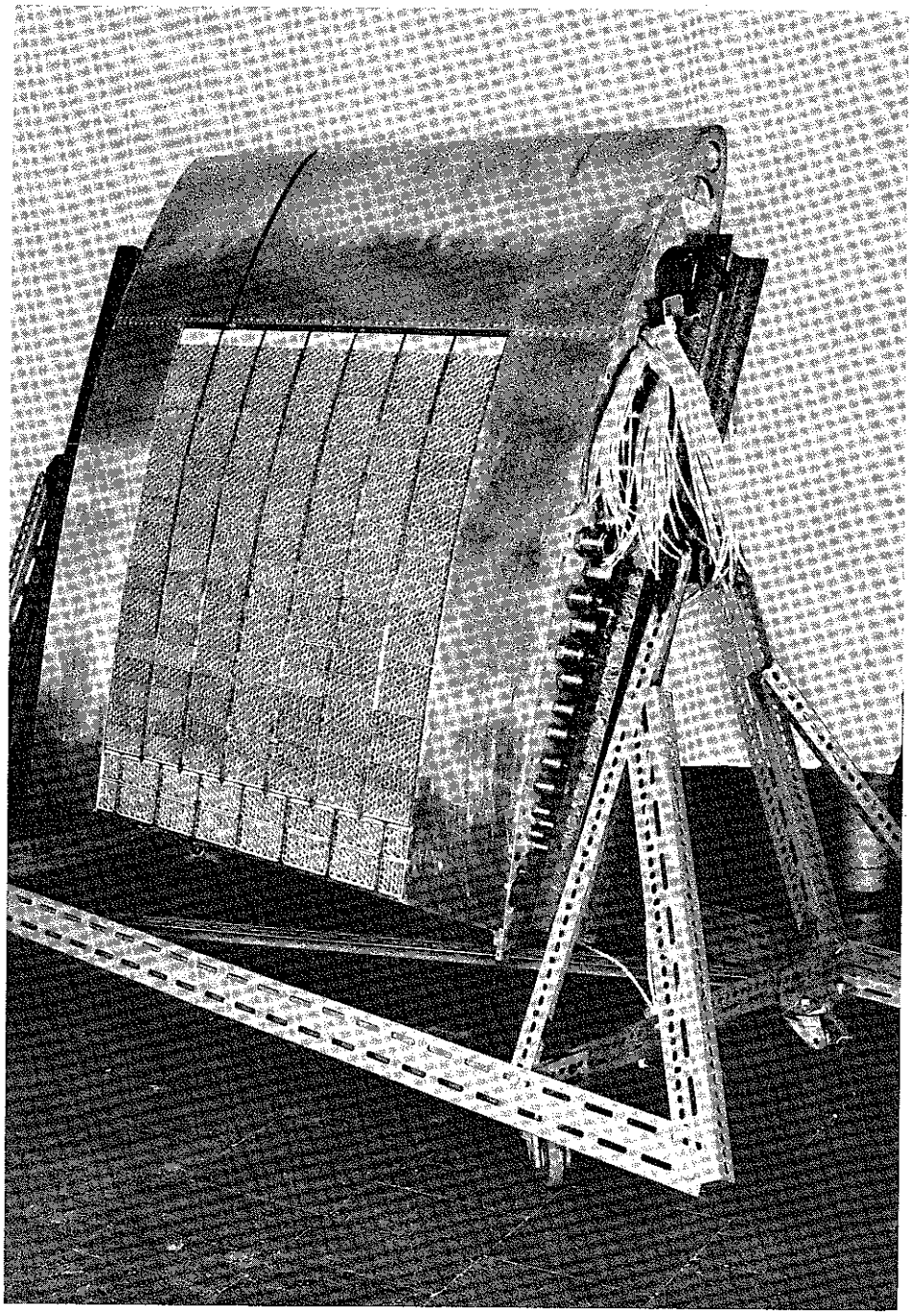

FIG. 11.5: MODEL COMPLETED EXCEPT FOR THE POROUS SURFACE AND TRAILING EDGE

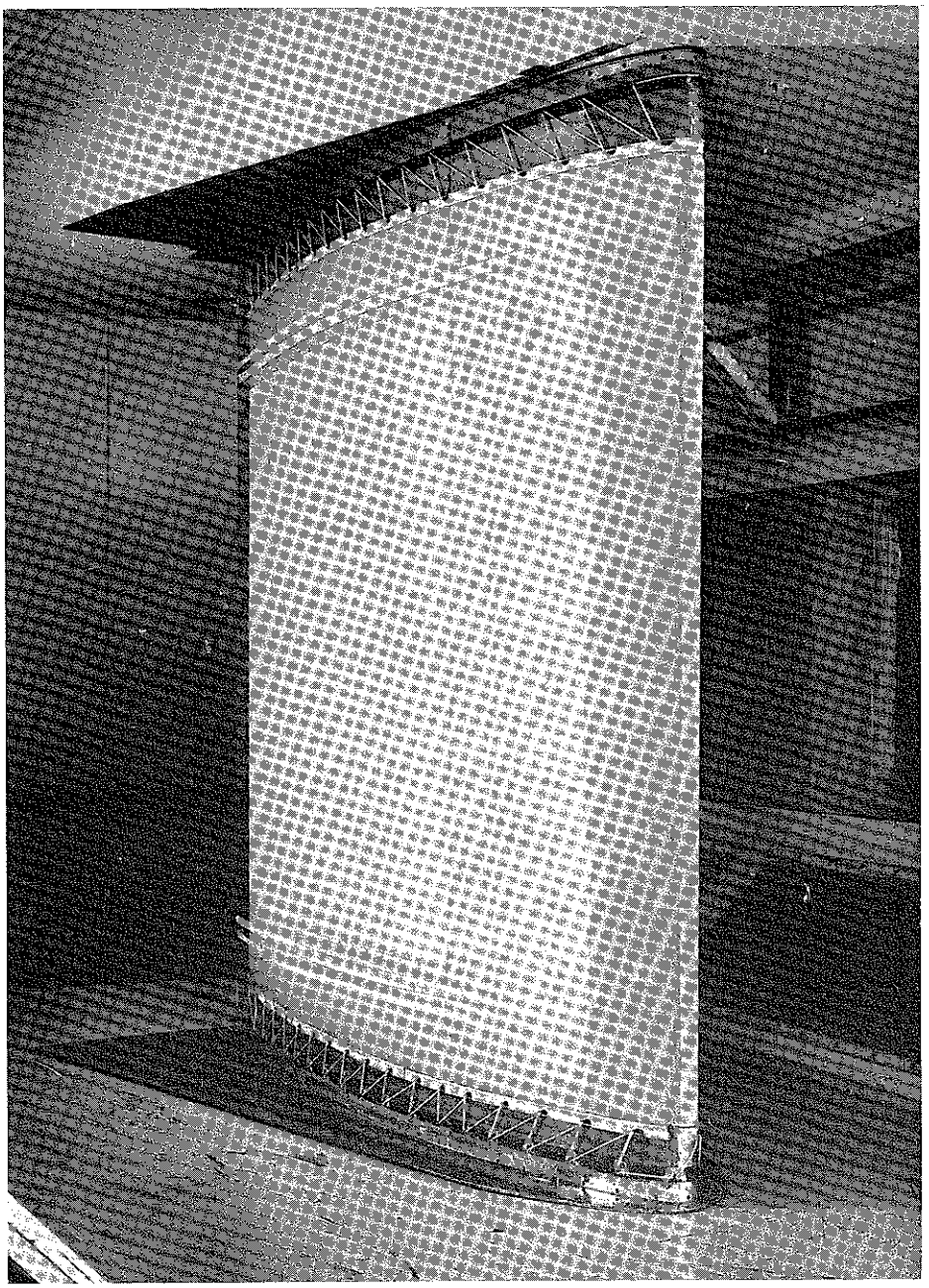

FIG. 11.6: MODEL INSTALLED IN TEST SECTION AND COVERED WITH NYLON

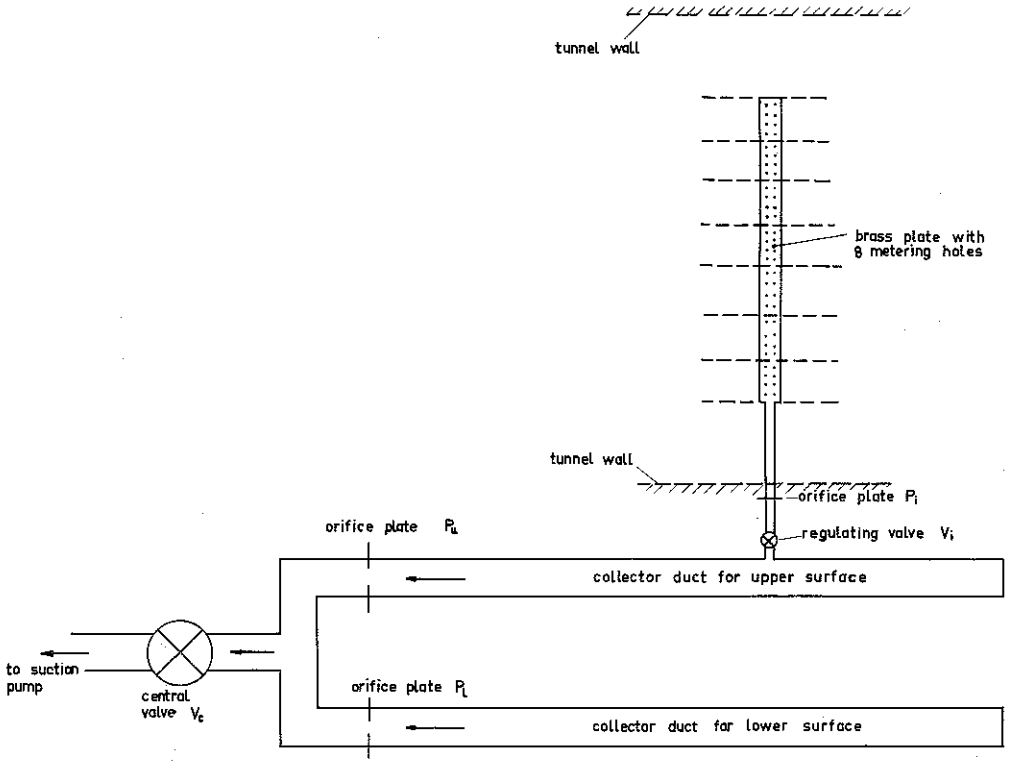

FIG. 11.7 : SCHEMATIC REPRESENTATION OF SUCTION INSTALLATION

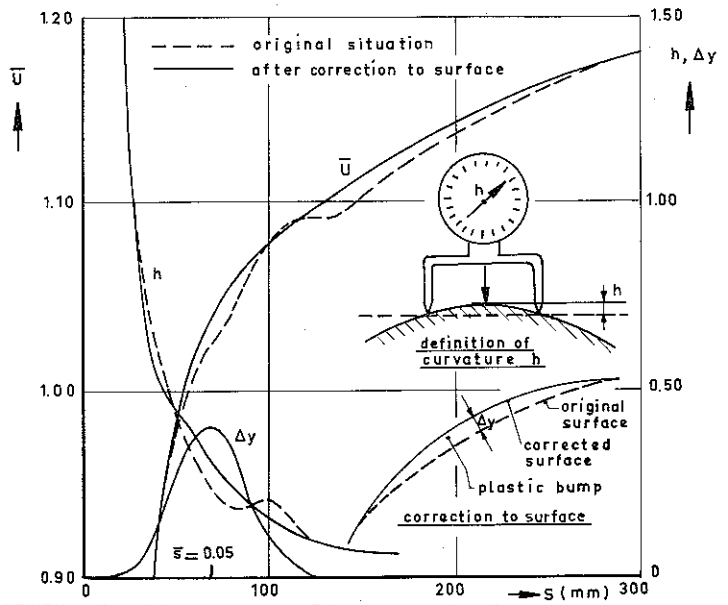

FIG. 11.8 : INFLUENCE OF CHANGES IN THE CURVATURE DISTRIBUTION ON $\bar{U}(s)$ FOR THE UPPER SURFACE

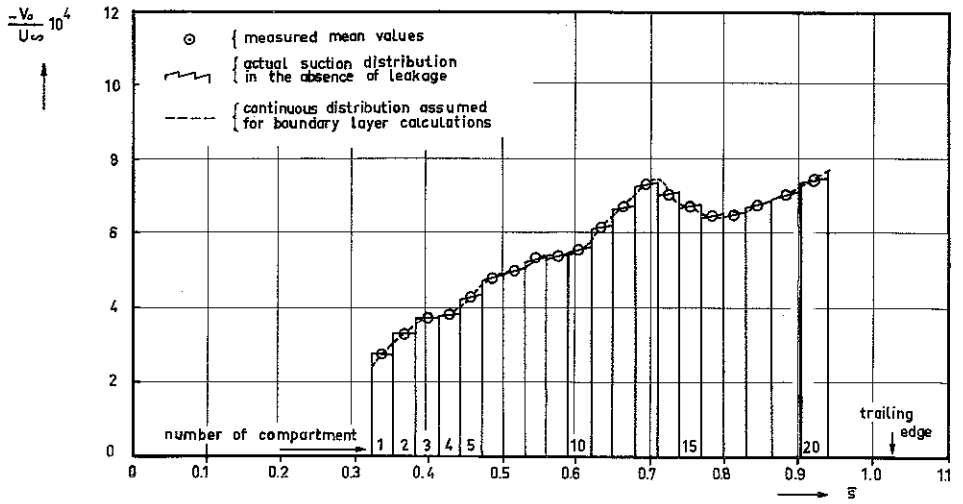

FIG. 11.9 : TYPICAL SUCTION DISTRIBUTION

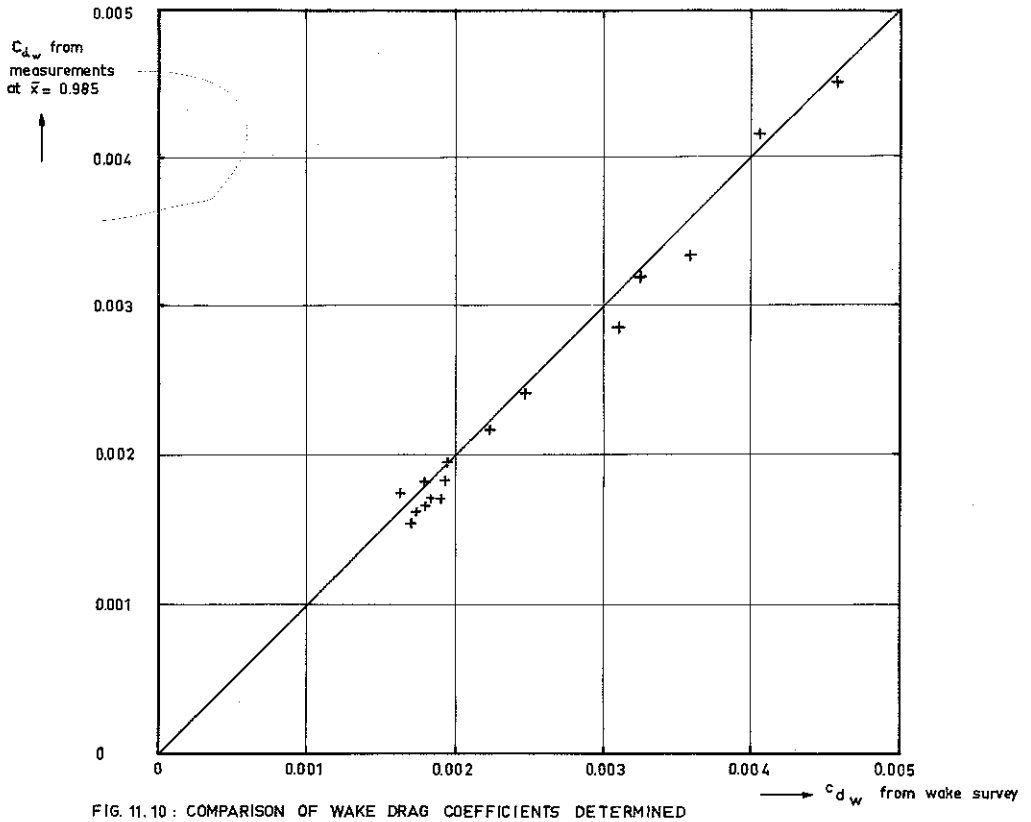

FIG. 11.10 : COMPARISON OF WAKE DRAG COEFFICIENTS DETERMINED FROM WAKE SURVEYS AND FROM BOUNDARY LAYER TRAVERSES AT $\bar{X}$ = 0.985

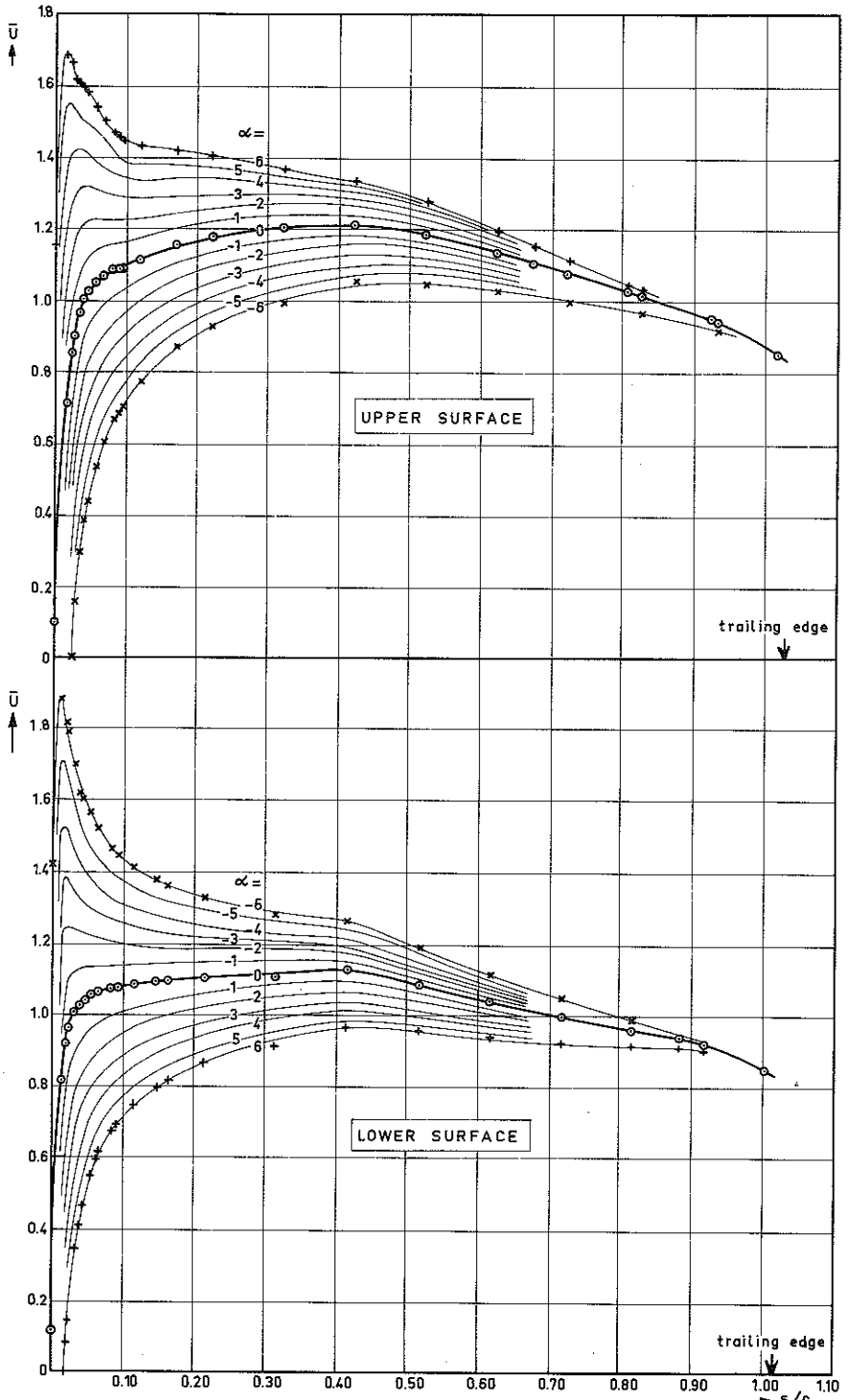

FIG. 11.11: MEASURED PRESSURE DISTRIBUTIONS IN TERMS OF $\bar{U}$; $R_c = 5.5 \times 10^6$.
(NOTE THAT NOT ALL DATA POINTS ARE SHOWN).

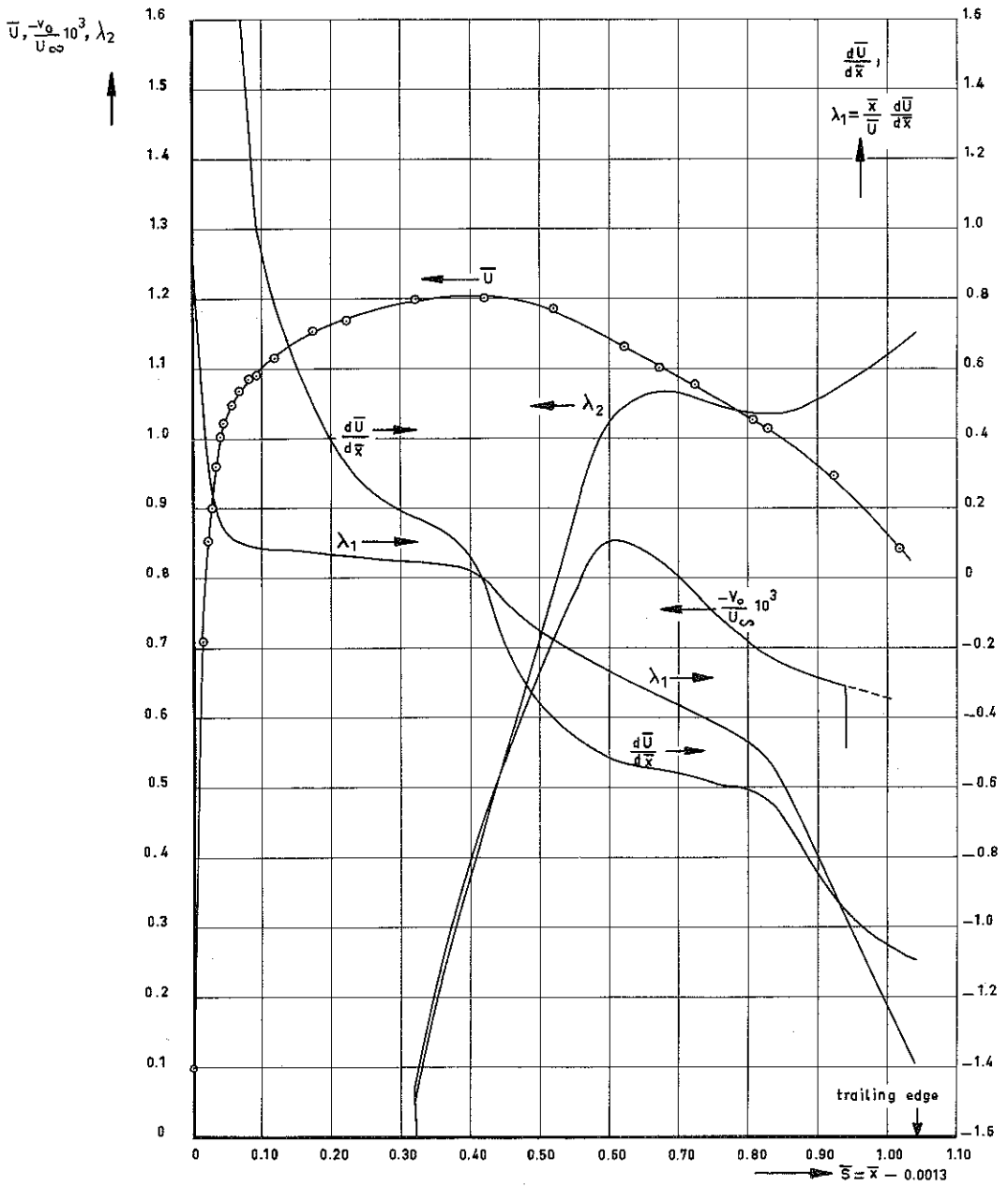

FIG.11.12: DETAILS OF PRESSURE—AND SUCTION DISTRIBUTIONS USED FOR BOUNDARY LAYER CALCULATIONS IN SECTION 11.5 (SEE ALSO TABLE 11.4)

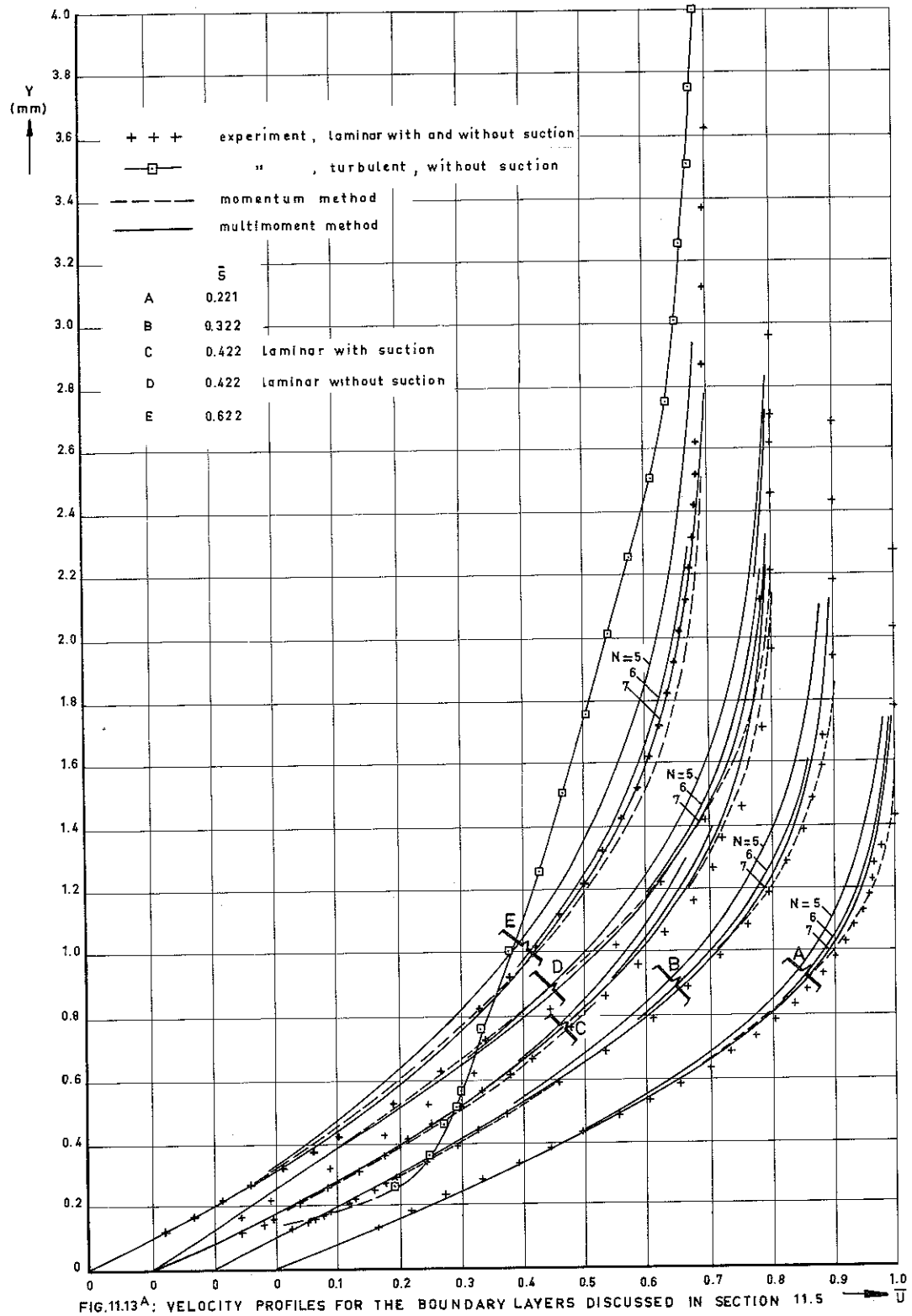

FIG.11.13[A]: VELOCITY PROFILES FOR THE BOUNDARY LAYERS DISCUSSED IN SECTION 11.5

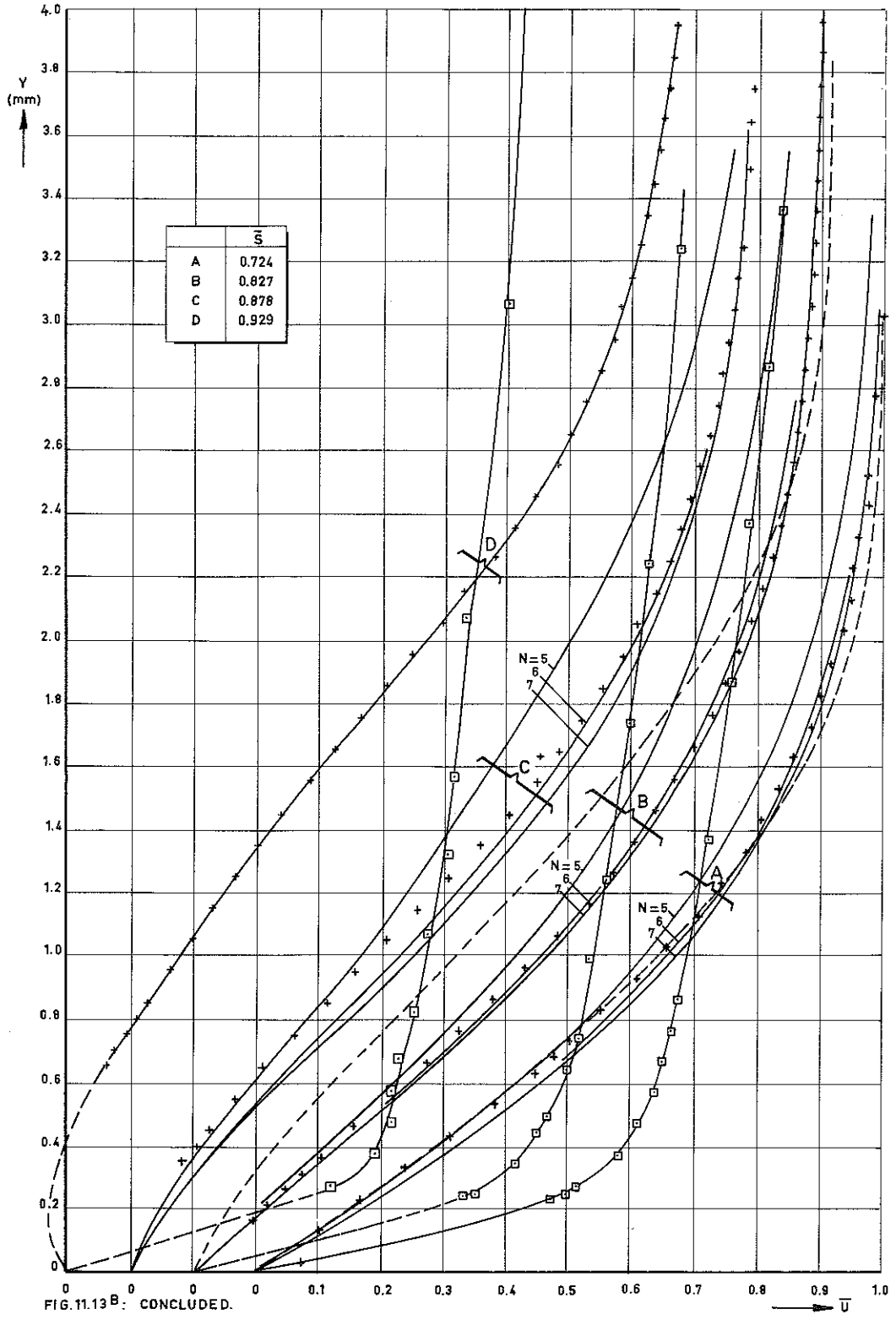

FIG. 11.13 B: CONCLUDED.

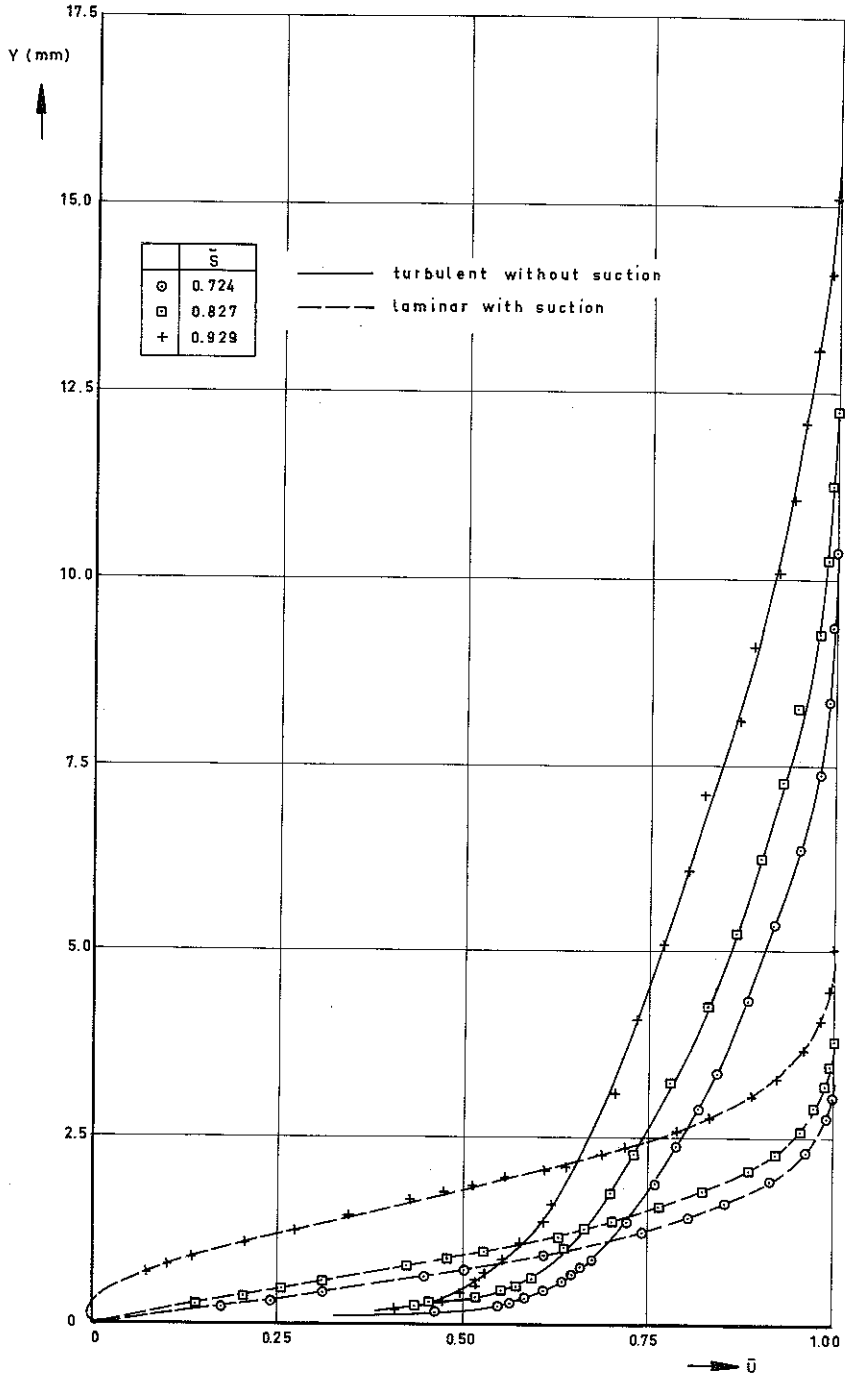

FIG. 11.14 : SOME VELOCITY PROFILES IN THE POROUS REGION WITH AND WITHOUT SUCTION.

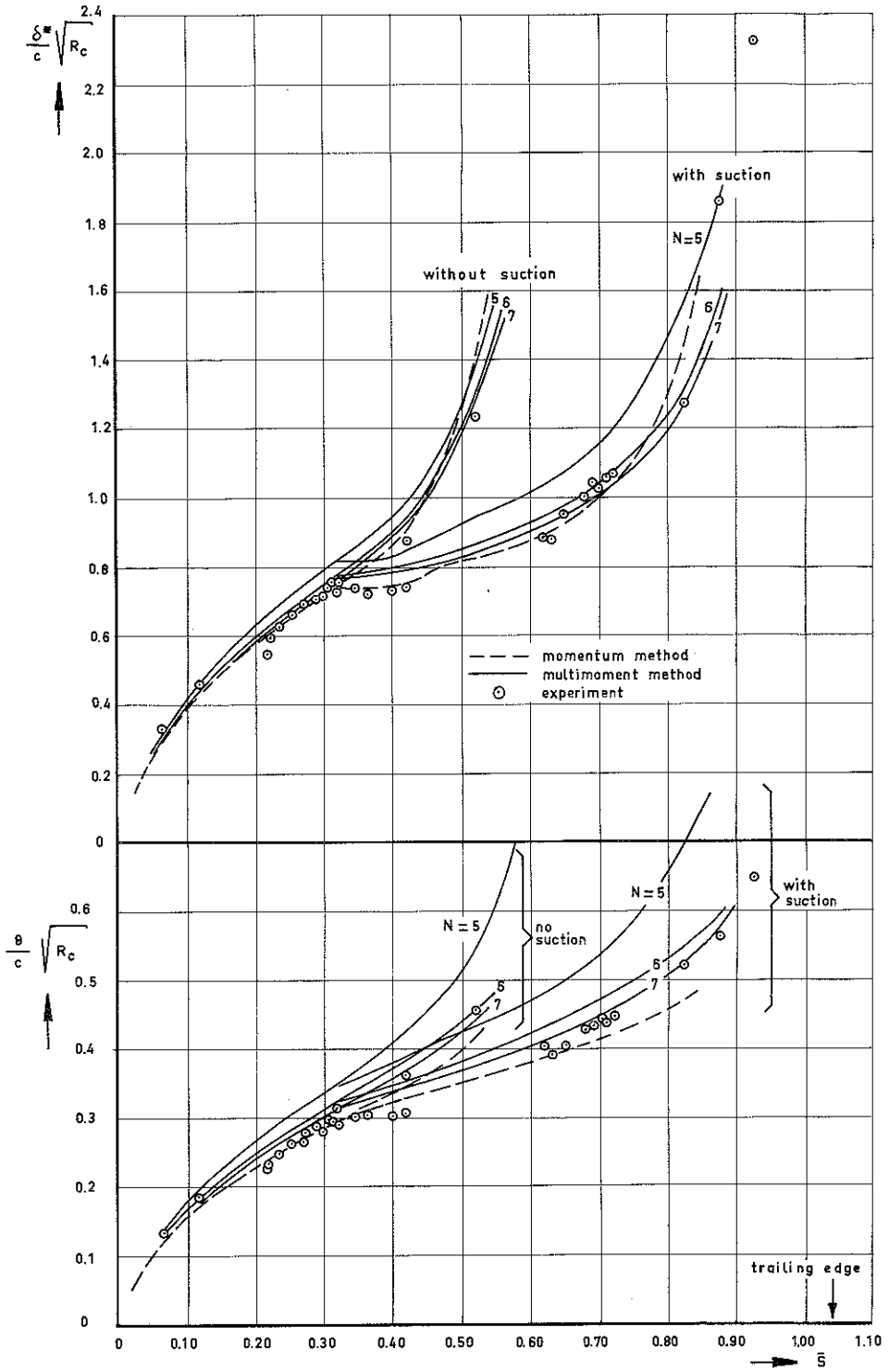

FIG. 11.15: DISPLACEMENT THICKNESS δ^* AND MOMENTUM LOSS THICKNESS θ FOR THE UPPER SURFACE WITH AND WITHOUT SUCTION ; $\alpha = 0$, $R_c = 2.75 \times 10^6$.

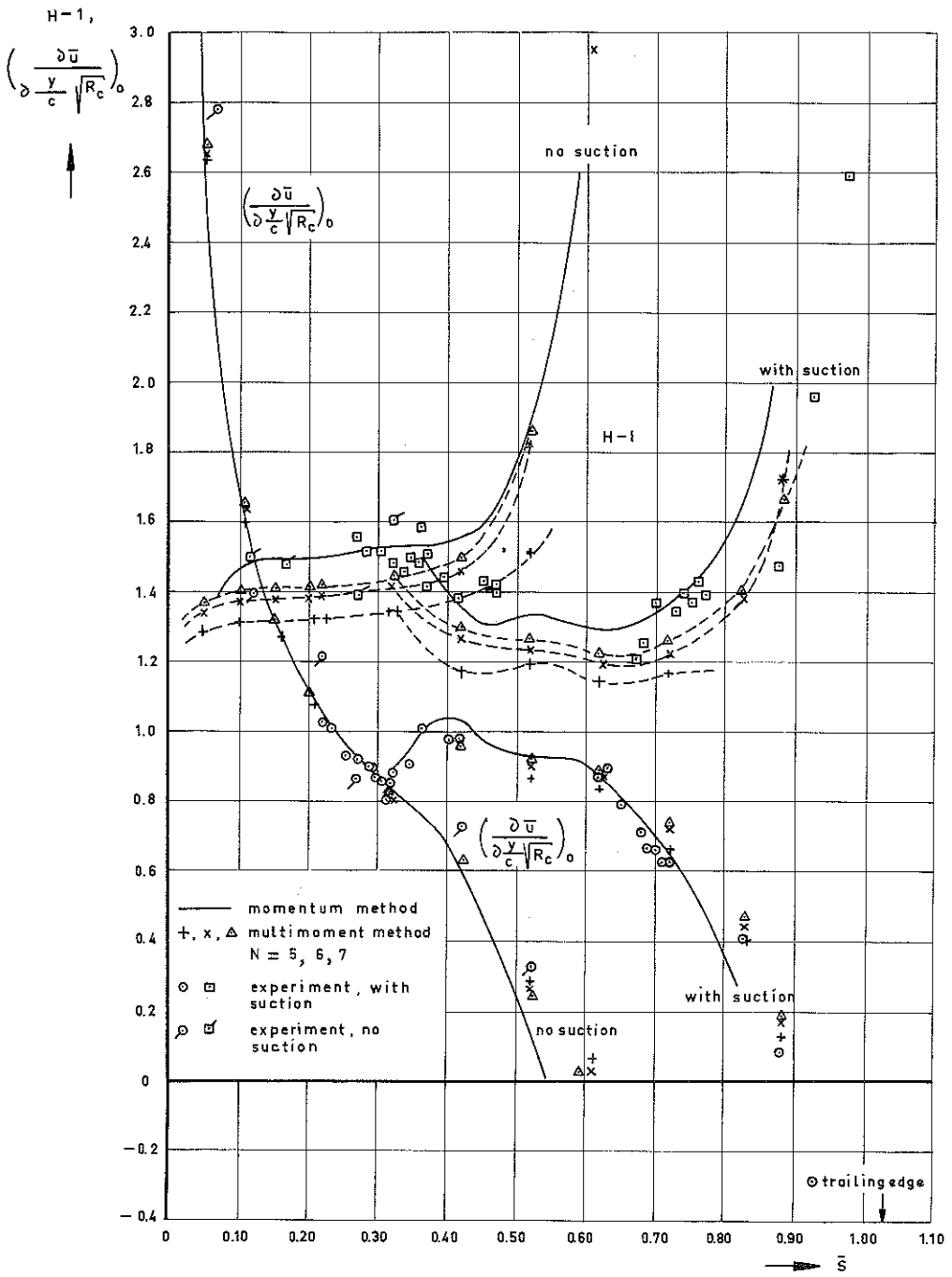

FIG. 11.16 : WALL SHEAR STRESS AND SHAPE FACTOR H FOR THE UPPER SURFACE WITH AND WITHOUT SUCTION ; $\alpha = 0$, $R_c = 2.75 \times 10^6$.

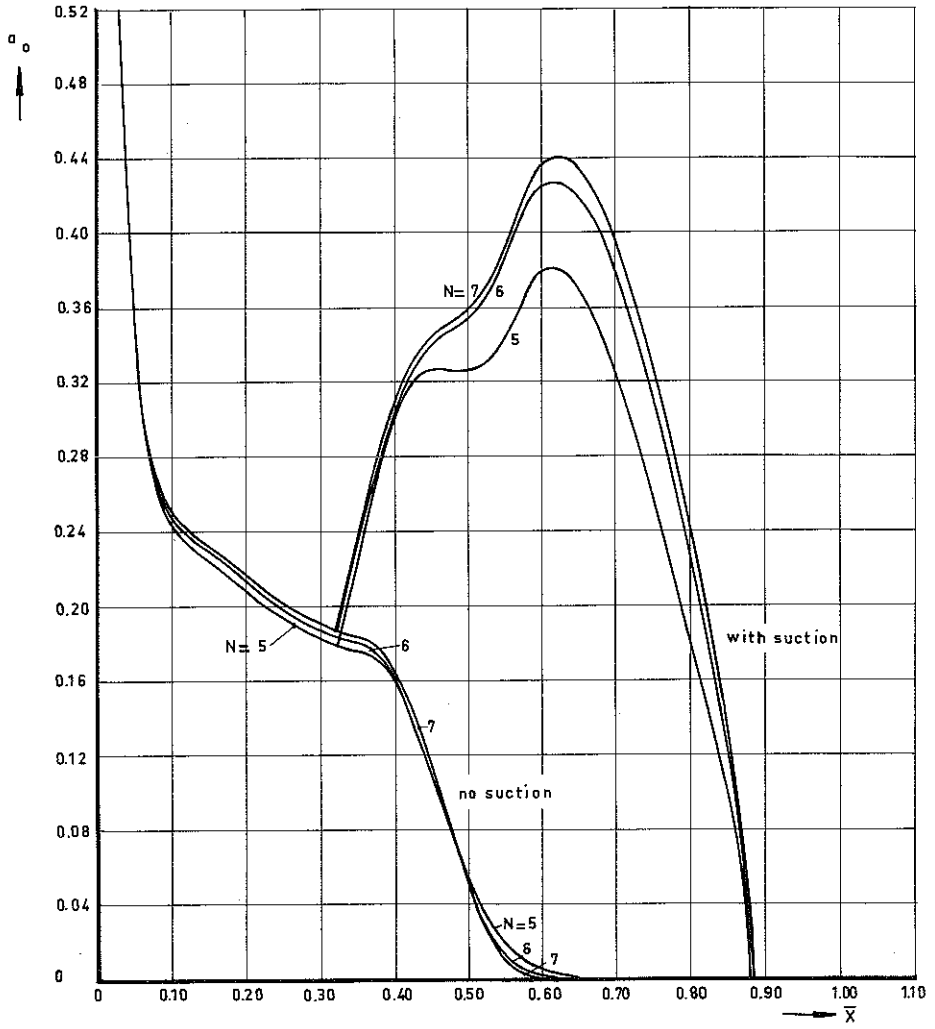

FIG. 11.17: THE SHEAR STRESS PARAMETER a_o FOR THE TWO BOUNDARY LAYERS DISCUSSED IN SECTION 11.5 ; CALCULATED WITH THE MULTIMOMENT METHOD

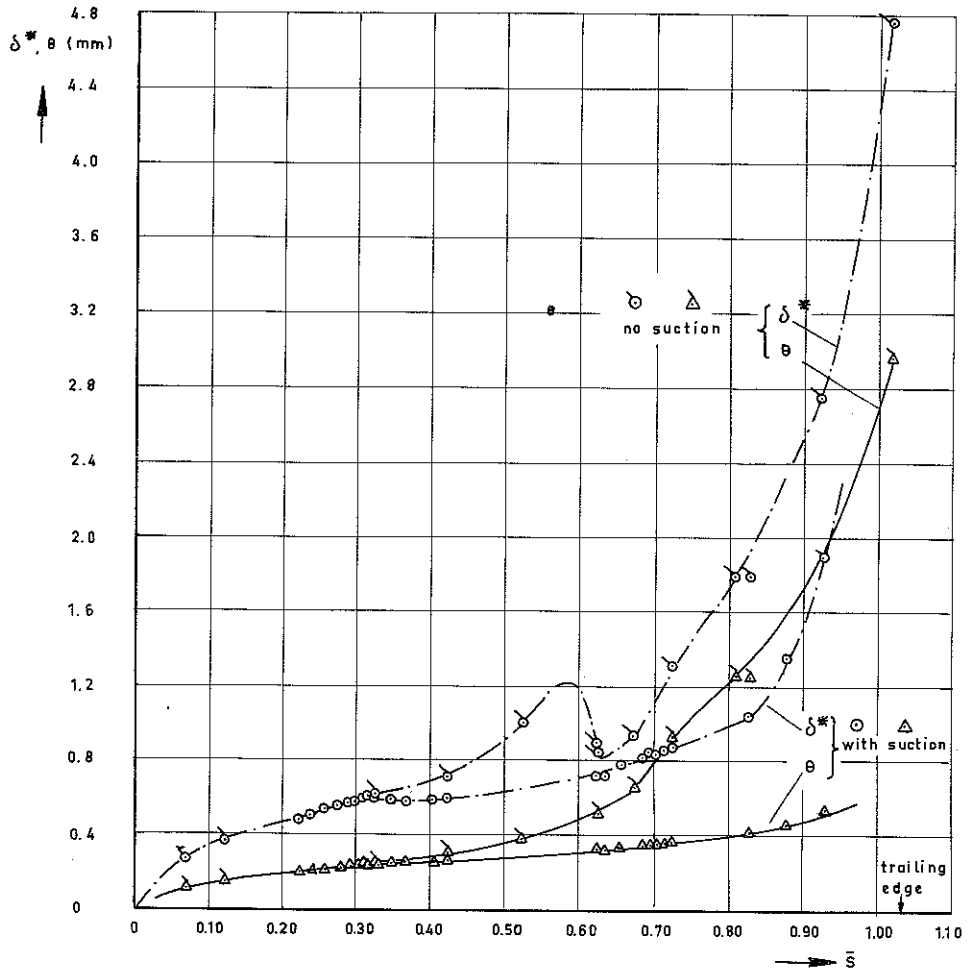

FIG.11.18 : δ^* AND θ FOR THE UPPER SURFACE WITH AND WITHOUT SUCTION ; $\alpha = 0$, $R_c = 2.75 \times 10^6$

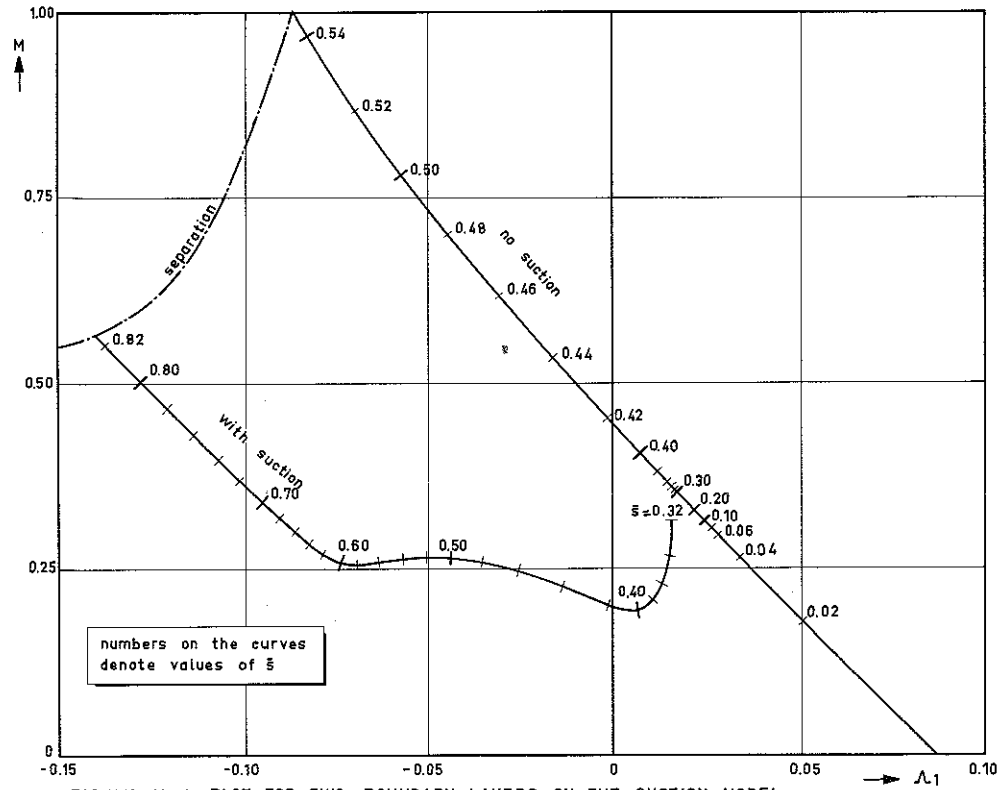

FIG. 11.19: M - Λ_1 PLOT FOR TWO BOUNDARY LAYERS ON THE SUCTION MODEL.

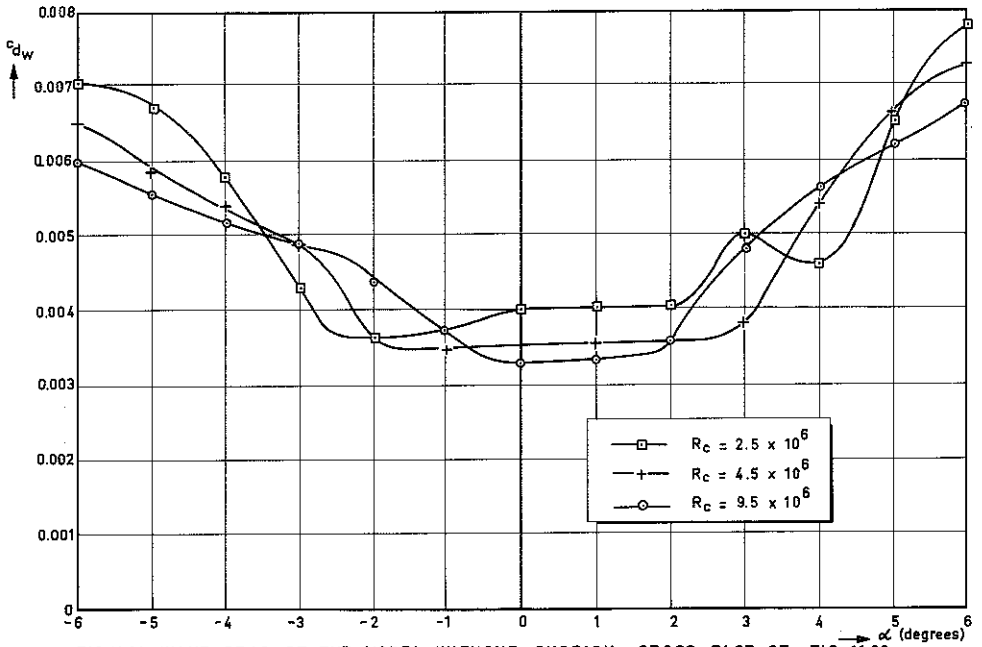

FIG. 11.21: WAKE DRAG OF THE MODEL WITHOUT SUCTION: CROSS PLOT OF FIG. 11.20.
(NOTE : FIG. 11.20 ON NEXT PAGE)

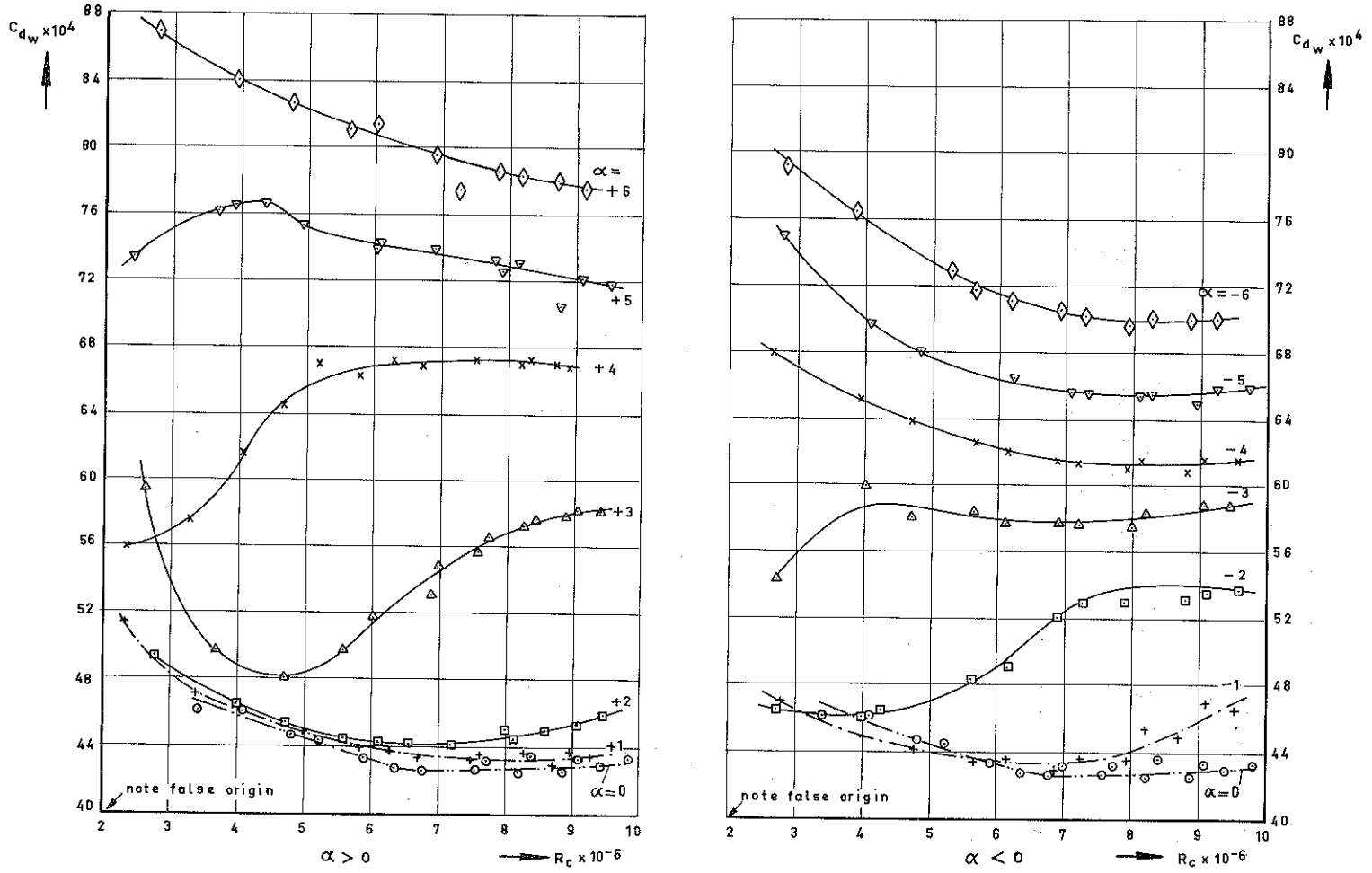

FIG.11.20: WAKE DRAG COEFFICIENTS FOR THE SEALED MODEL DETERMINED FROM WAKE TRAVERSES

(NOTE FIG.11.21 ON PREVIOUS PAGE)

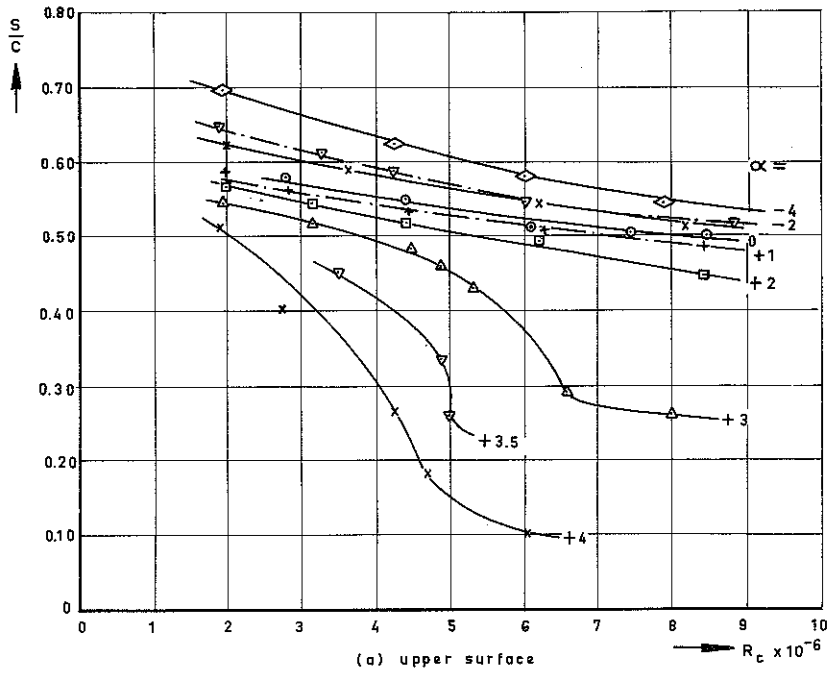

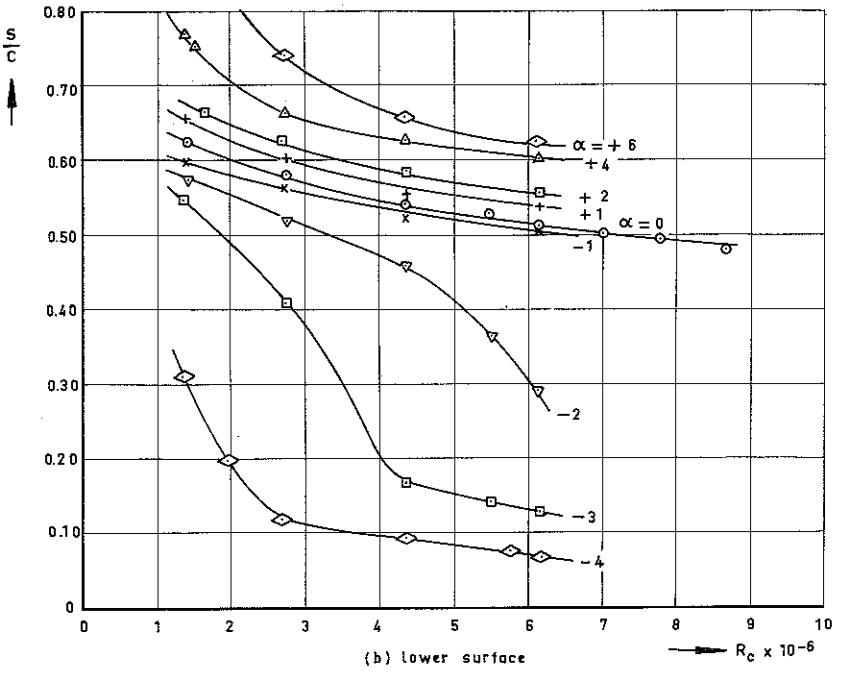

FIG.11.22: BEGINNING OF THE TRANSITION POSITION FOR THE SEALED MODEL

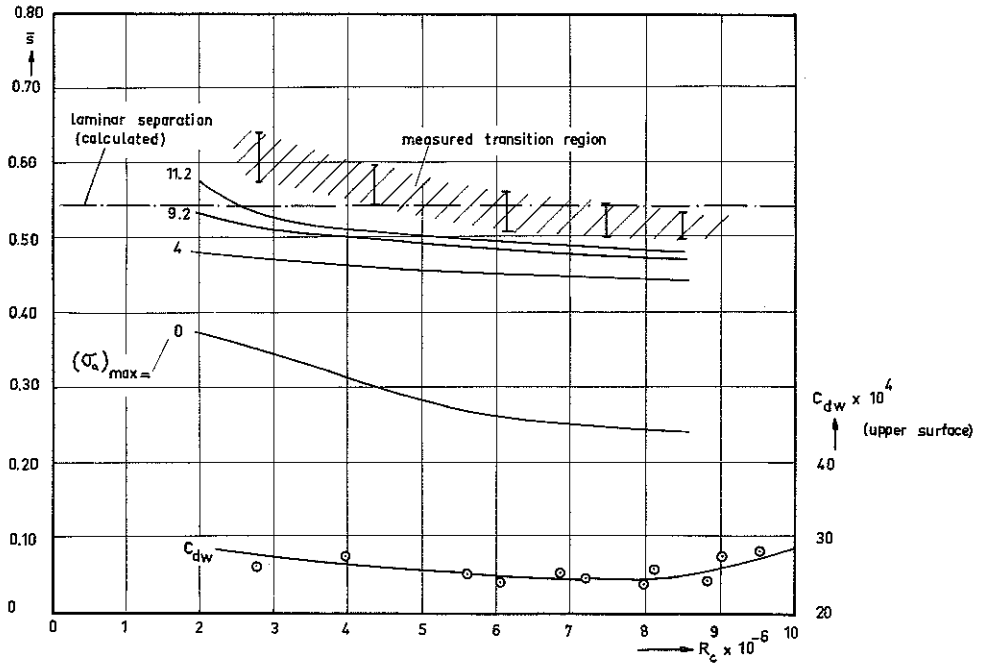

FIG. 11.23. TRANSITION AND DRAG FOR THE UPPER SURFACE

$\alpha = 0°$; NO SUCTION.

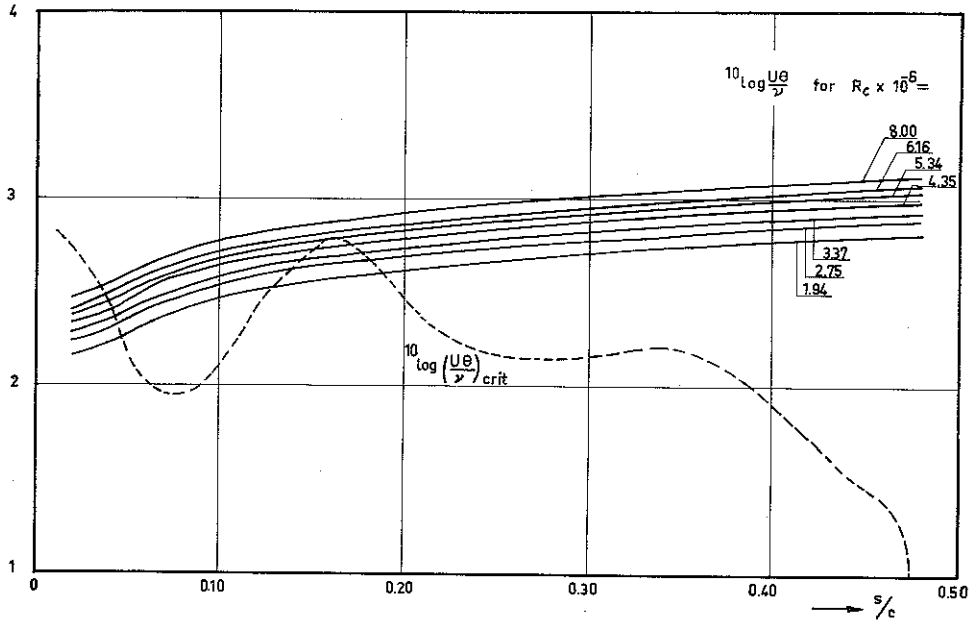

FIG. 11.24. RESULTS OF BOUNDARY LAYER CALCULATIONS WITH THE MOMENTUM METHOD; UPPER SURFACE, $\alpha = +3°$, NO SUCTION.

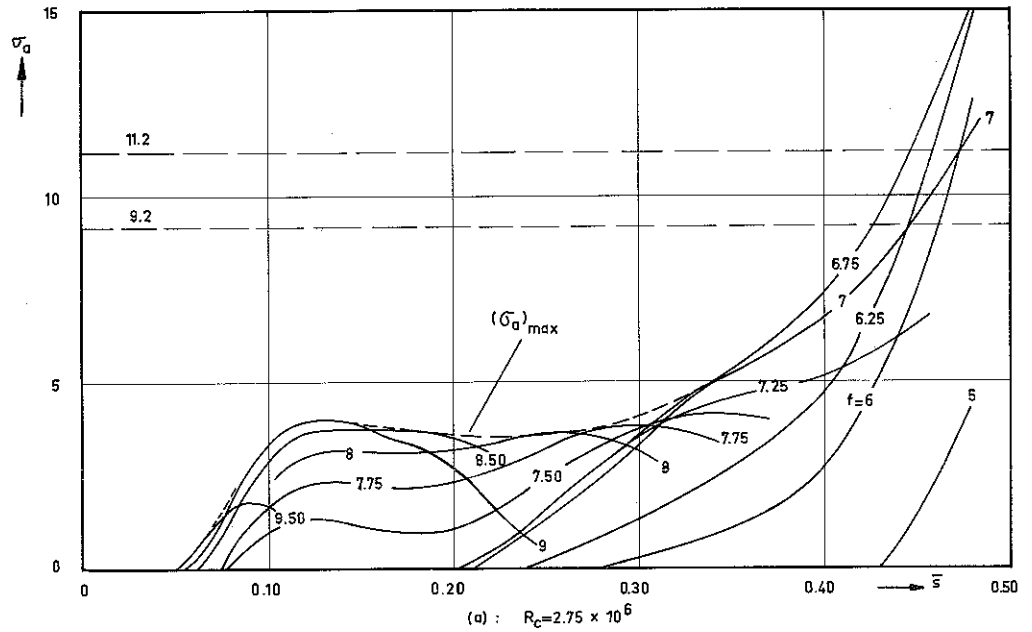

(a) : $R_c = 2.75 \times 10^6$

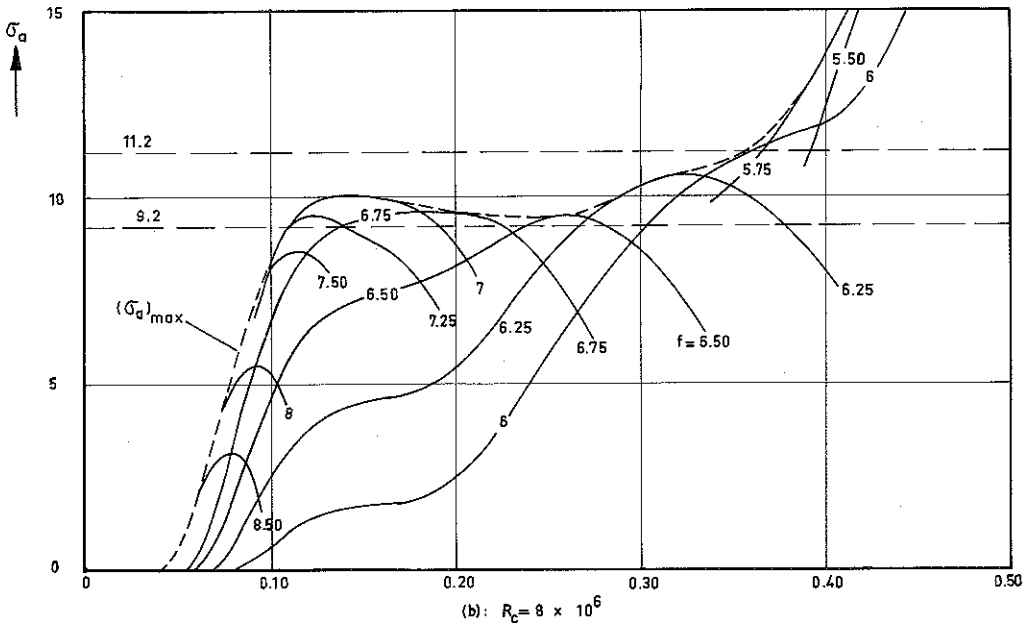

(b): $R_c = 8 \times 10^6$

FIG. 11.25: RESULTS OF AMPLIFICATION CALCULATIONS FOR THE UPPER SURFACE ; $\alpha = 3^\circ$; NO SUCTION.
(numbers on the curves denote values of the frequency parameter f)

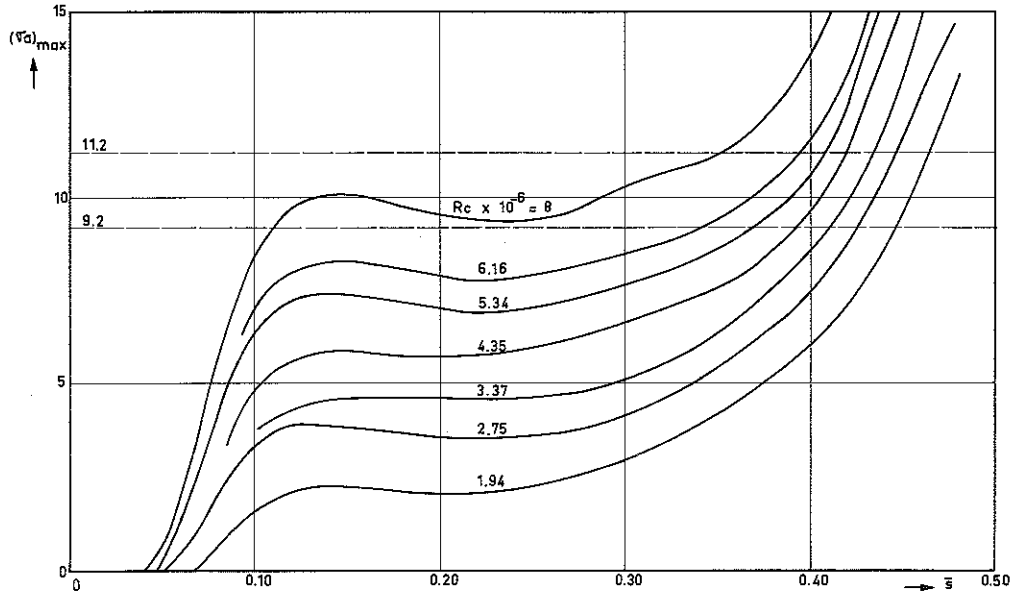

FIG. 11.26: MAXIMUM AMPLIFICATION FACTOR FOR THE UPPER SURFACE AT DIFFERENT VALUES OF R_c ; $\alpha = 3°$; NO SUCTION.

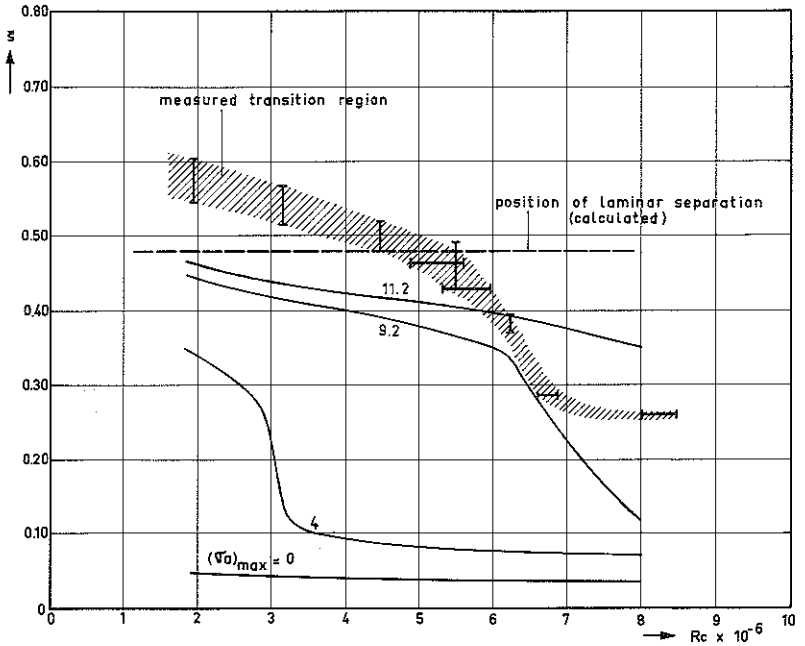

FIG. 11.27: MEASURED TRANSITION REGION AND CALCULATED AMPLIFICATION FACTORS FOR THE UPPER SURFACE WITHOUT SUCTION; $\alpha = 3°$.

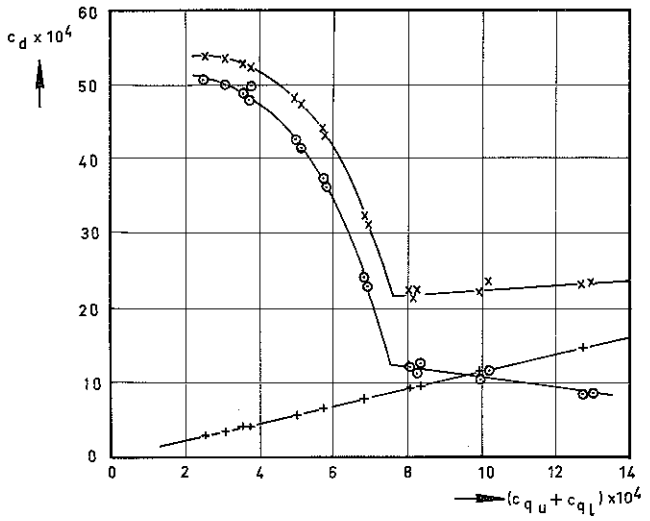

FIG. 11.28: UPPER+LOWER SURFACE

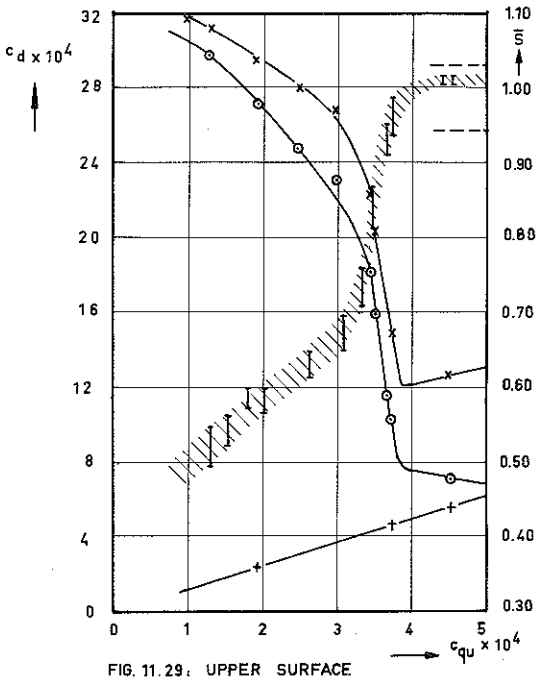

FIG. 11.29: UPPER SURFACE

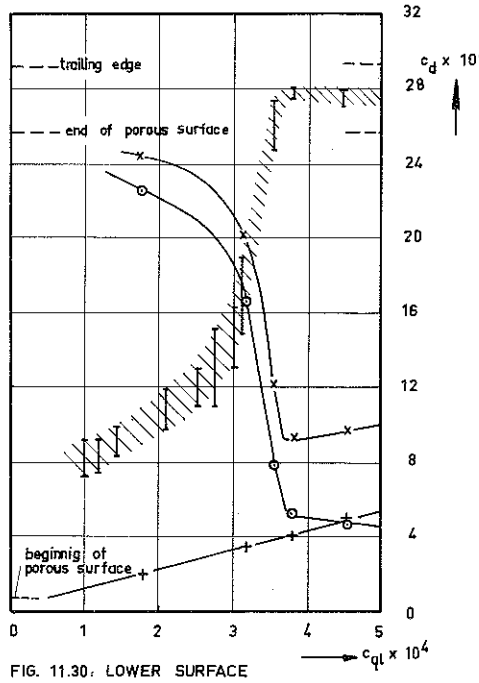

FIG. 11.30: LOWER SURFACE

FIG. 11.28–11.30: TRANSITION AND DRAG WITH SUCTION; SERIES 1

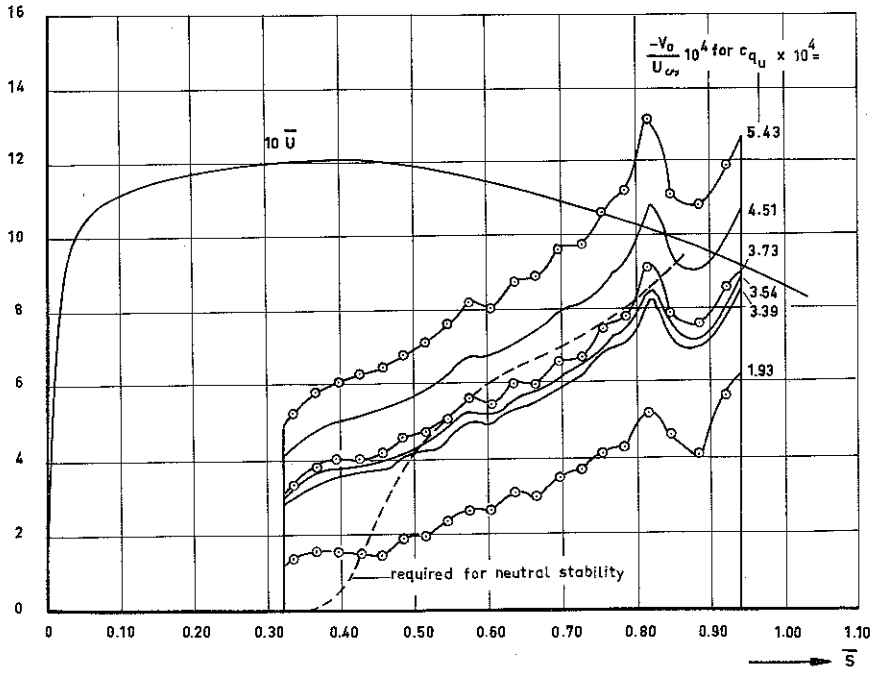

FIG. 11.31 : SUCTION VELOCITY DISTRIBUTIONS FOR THE UPPER SURFACE ; $\alpha = 0$, SERIES 1.

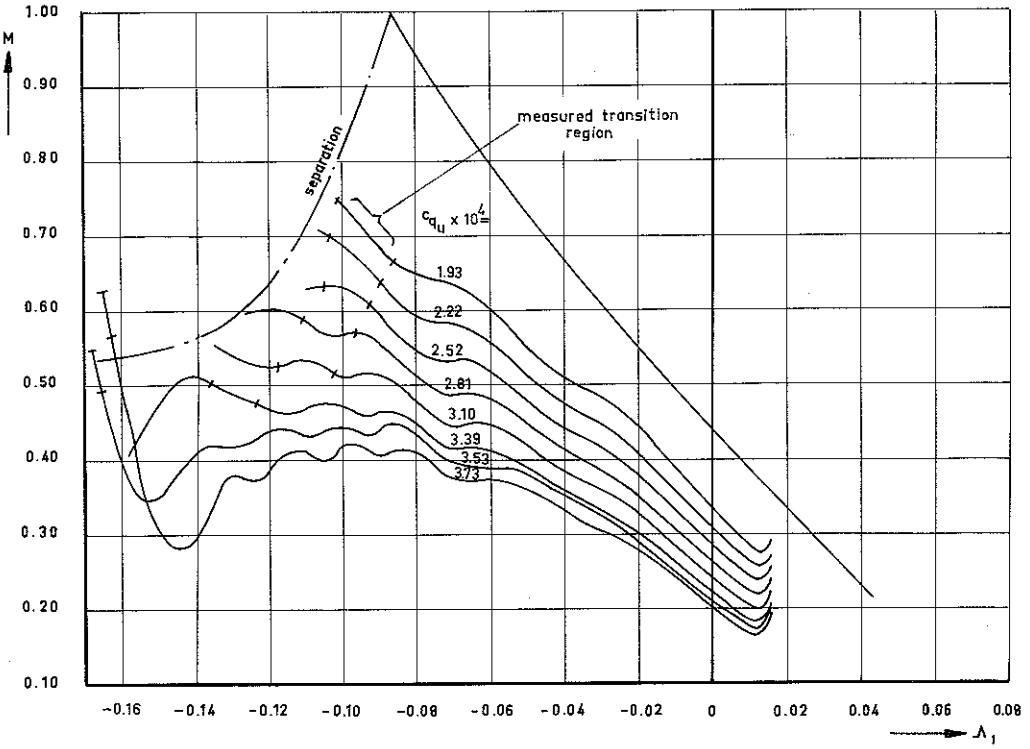

FIG. 11.32 : M − Λ_1 PLOT FOR THE UPPER SURFACE , SERIES 1.

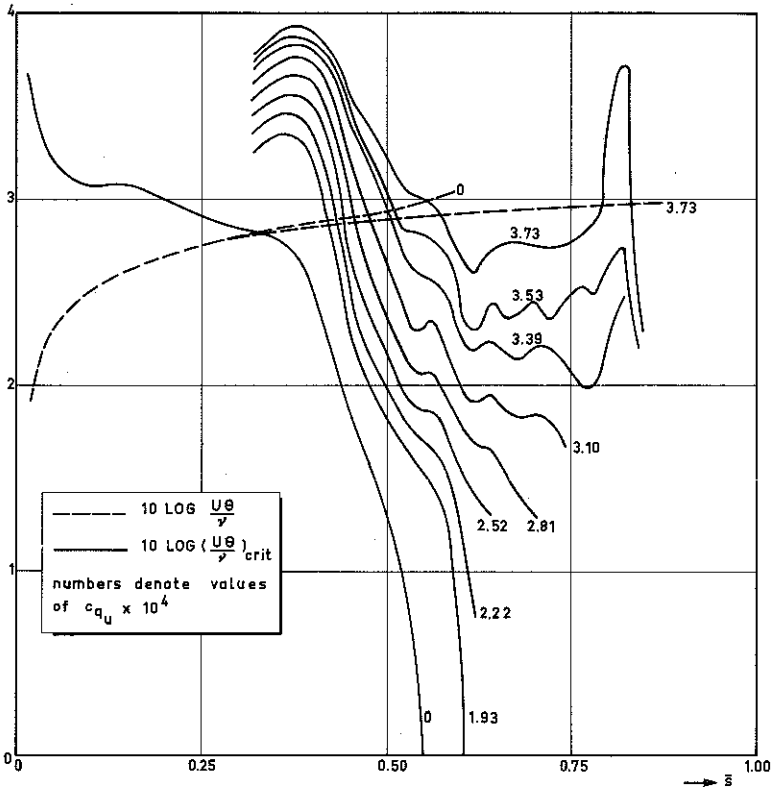

FIG. 11.33: 10 LOG $\frac{U\theta}{\nu}$ AND 10 LOG $(\frac{U\theta}{\nu})_{crit}$ FOR THE UPPER SURFACE; SERIES 1.

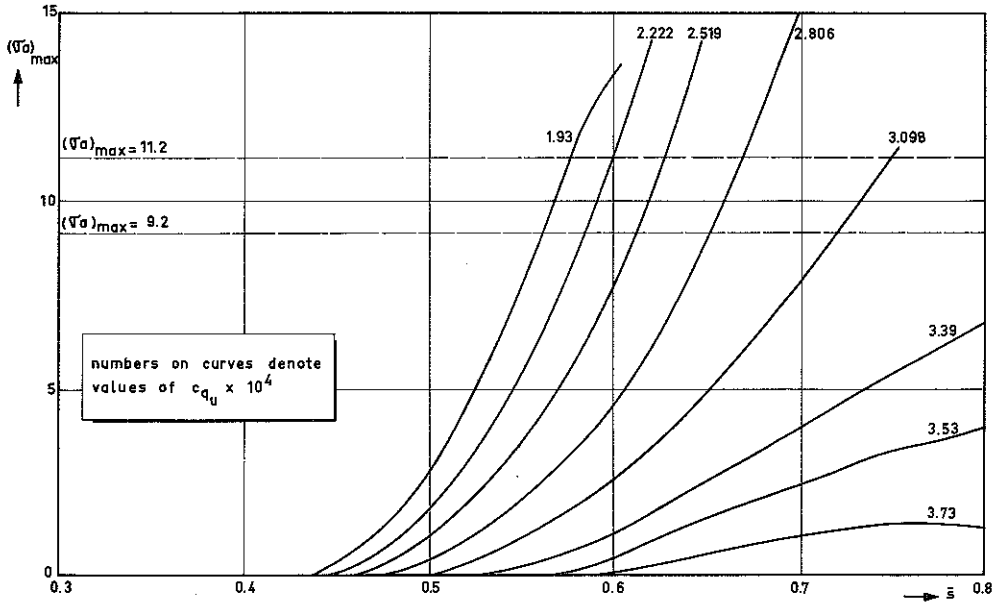

FIG. 11.34: $(\Gamma a)_{max}$ FOR DIFFERENT VALUES OF $c_{q_u} \times 10^4$; UPPER SURFACE, SERIES 1.

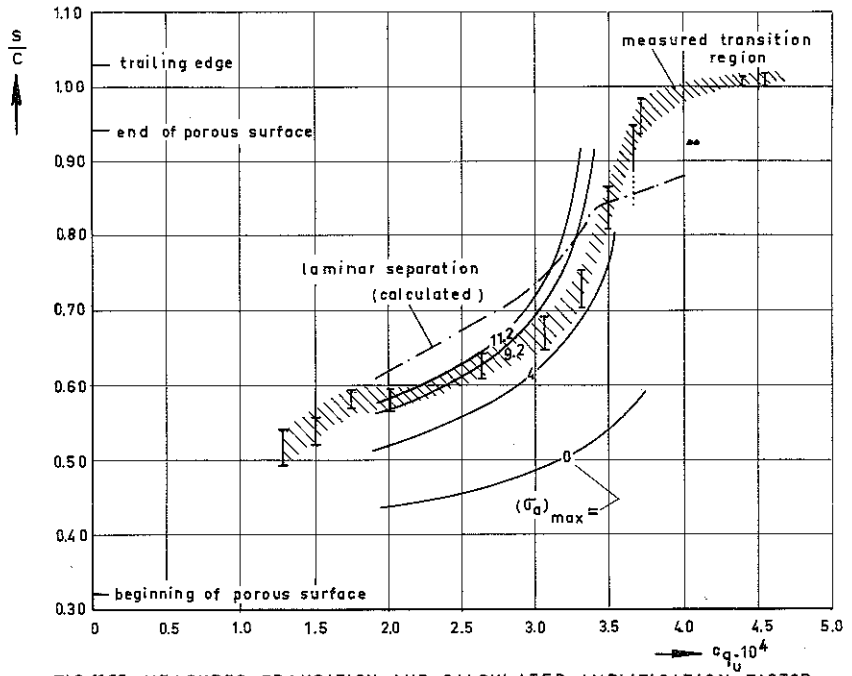

FIG.11.35: MEASURED TRANSITION AND CALCULATED AMPLIFICATION FACTOR FOR THE UPPER SURFACE OF THE SUCTION MODEL, $\alpha = 0°$, $R_c = 3.37 \times 10^6$ SERIES 1.

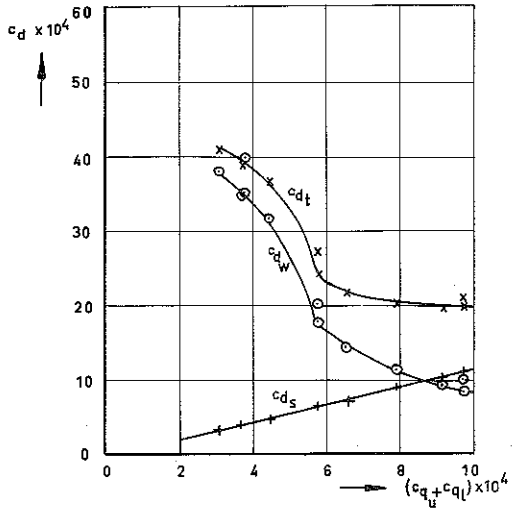

FIG.11.36: TRANSITION AND DRAG UPPER + LOWER SURFACE, SERIES 2.

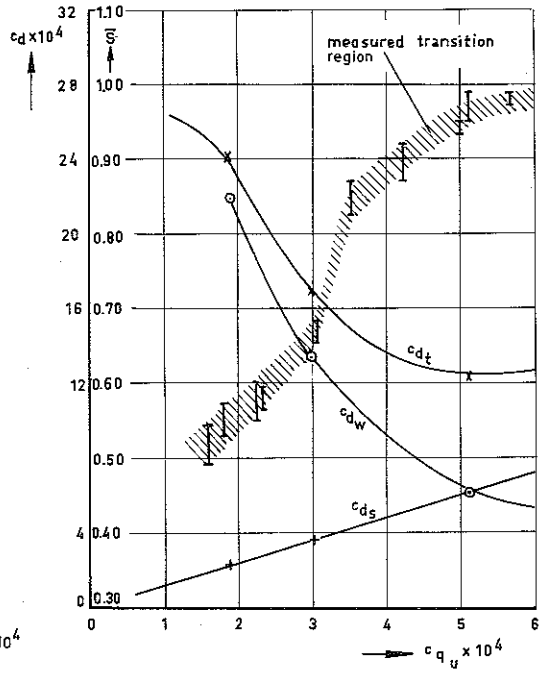

FIG.11.37: TRANSITION AND DRAG; UPPER SURFACE SERIES 2.

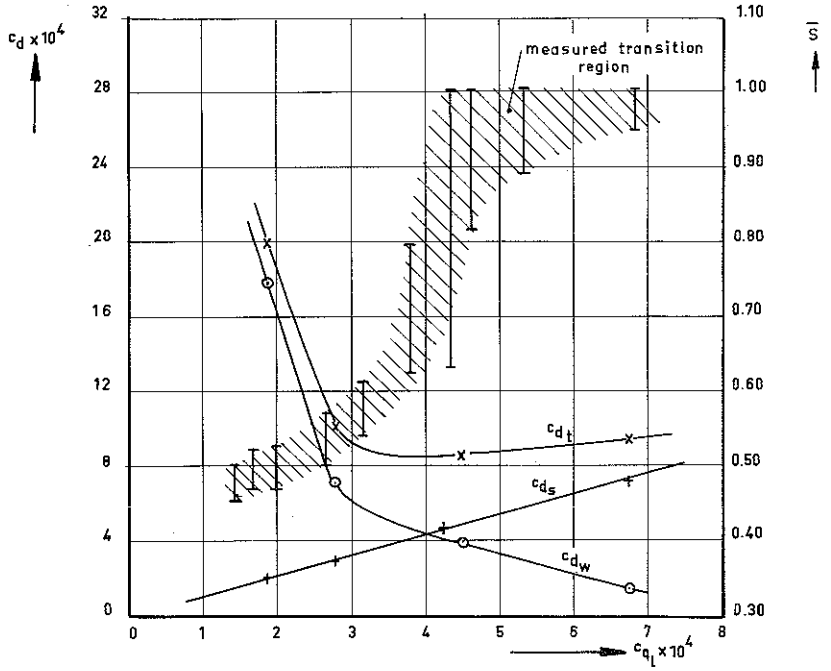

FIG.11.38 : TRANSITION AND DRAG FOR THE LOWER SURFACE ; SERIES 2.

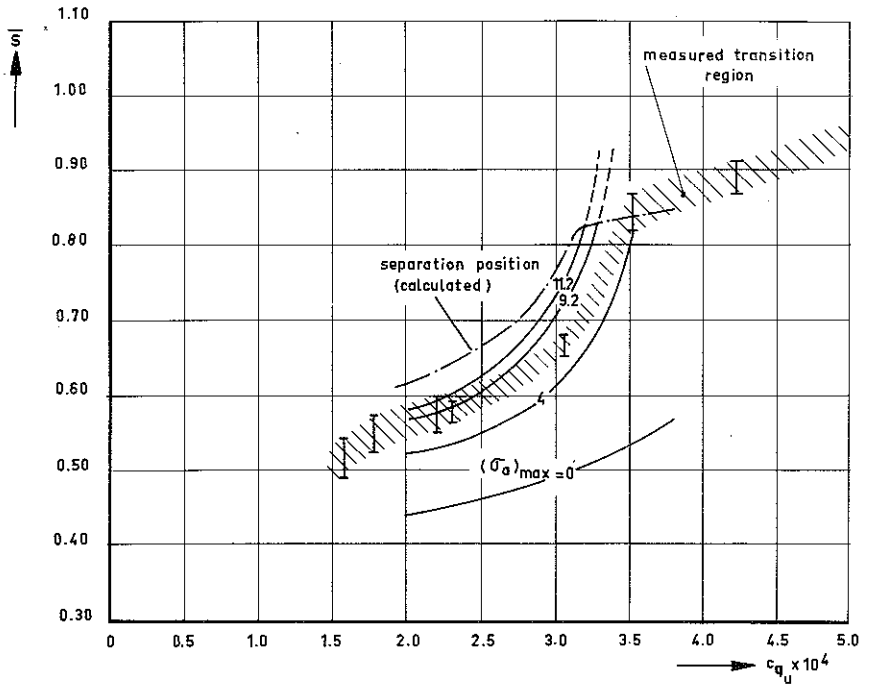

FIG.11.39 : MEASURED TRANSITION REGION AND CALCULATED AMPLIFICATION FACTOR FOR THE UPPER SURFACE , SERIES 2 .

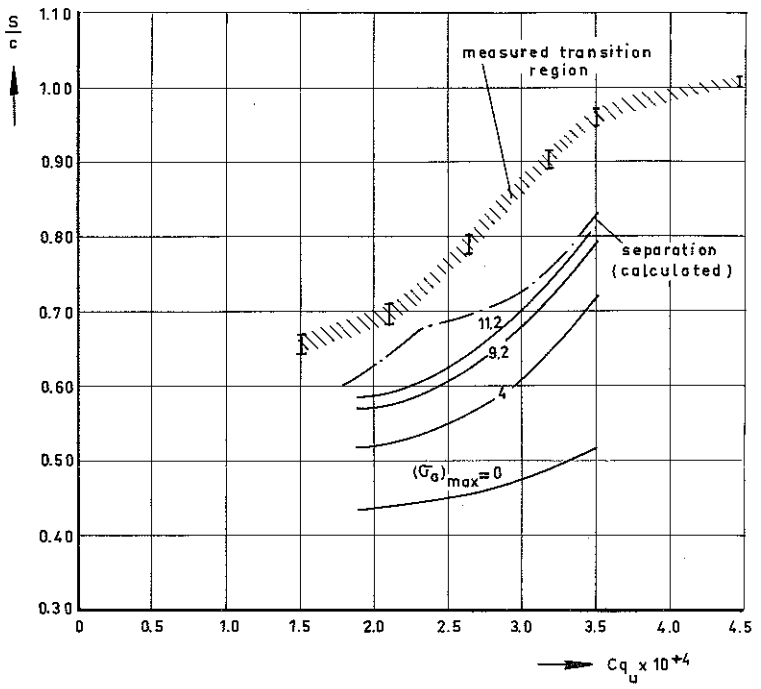

FIG. 11.40 : MEASURED TRANSITION AND CALCULATED AMPLIFICATION FACTOR FOR THE UPPER SURFACE ; $\alpha = 0$; SERIES 3 .

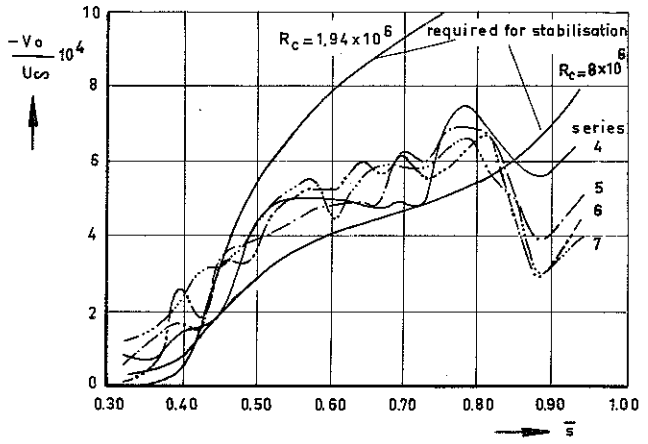

FIG.11.41 : SUCTION DISTRIBUTIONS FOR SERIES 4-7 ; TRANSITION AT THE END OF THE POROUS SURFACE.

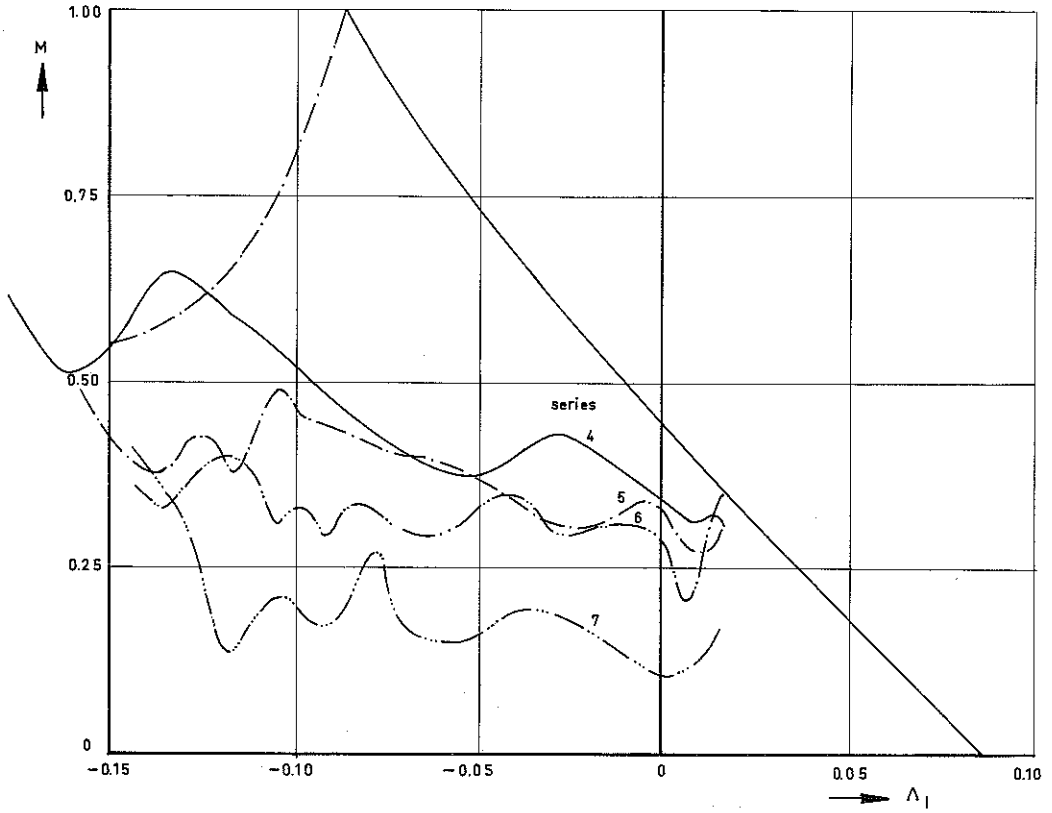

FIG.11.42: M−Λ_1 PLOTS FOR THE SUCTION DISTRUBUTIONS SHOWN IN FIG. 11.41

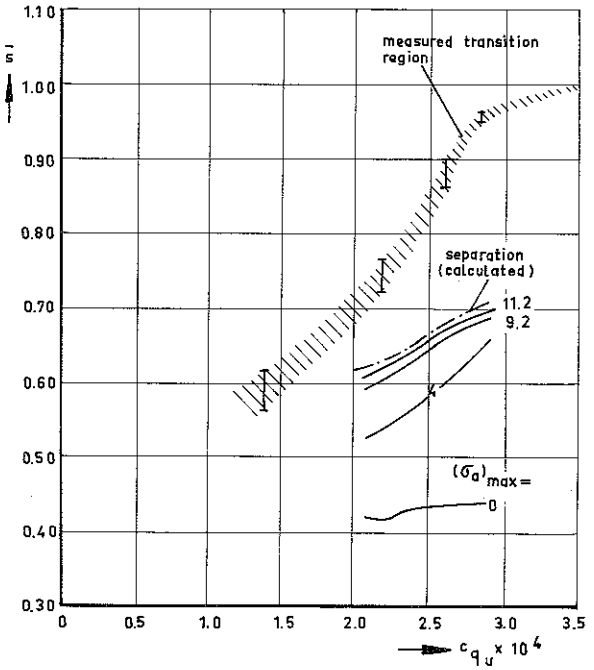

FIG.11.43: MEASURED TRANSITION REGION AND CALCULATED AMPLIFICATION FACTORS FOR THE UPPER SURFACE, SERIES 4.

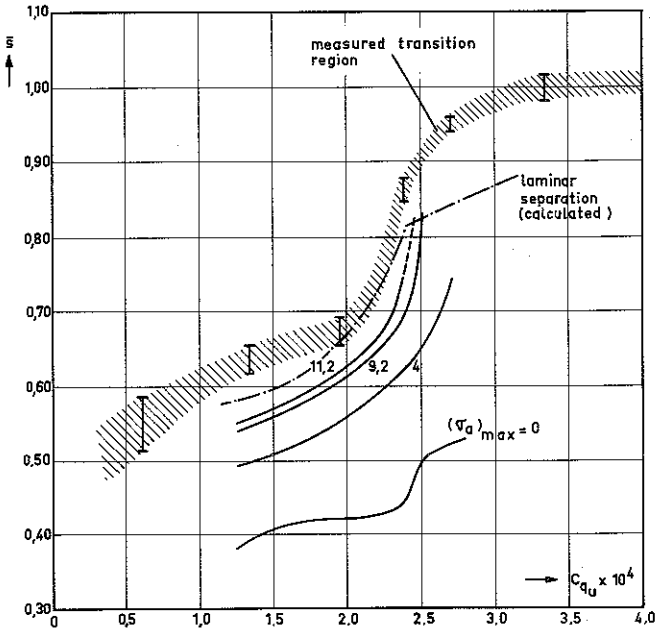

FIG. 11.44: MEASURED TRANSITION REGION AND CALCULATED AMPLIFICATION FACTORS FOR THE UPPER SURFACE, SERIES 5.

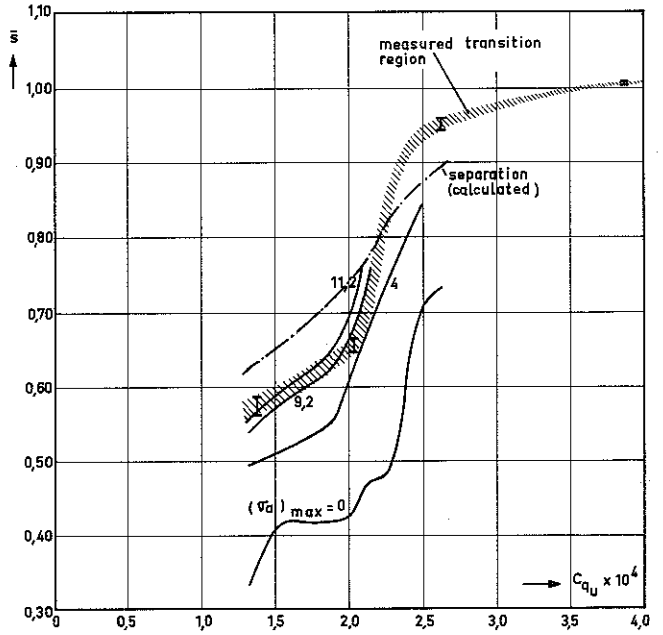

FIG. 11.45: MEASURED TRANSITION REGION AND CALCULATED AMPLIFICATION FACTORS FOR THE UPPER SURFACE, SERIES 6.

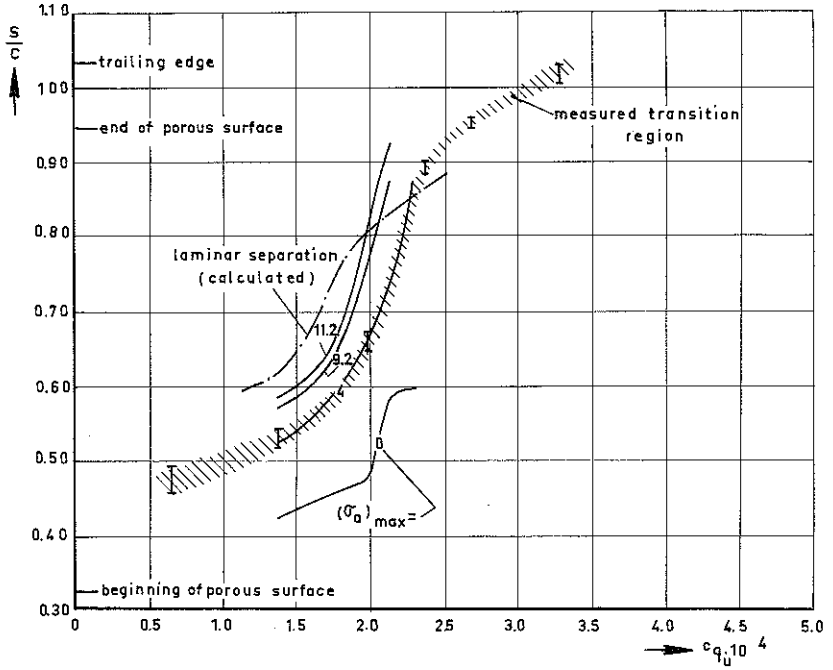

FIG.11.46: MEASURED TRANSITION AND CALCULATED AMPLIFICATION FACTOR FOR THE UPPER SURFACE OF THE SUCTION MODEL ; $\alpha = 0°$, $R_c = 6.16 \times 10^6$, SERIES 7

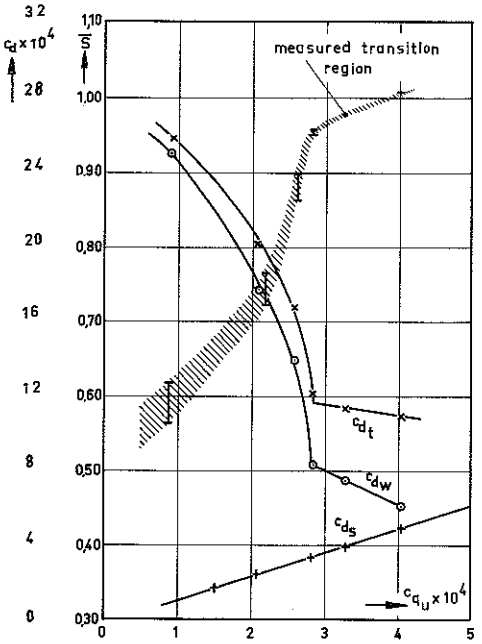

FIG.11.47: TRANSITION AND DRAG FOR THE UPPER SURFACE, SERIES 4.

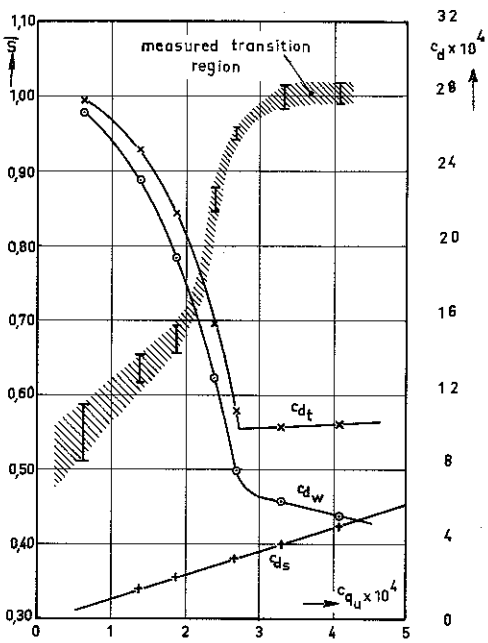

FIG.11.48 : TRANSITION AND DRAG FOR THE UPPER SURFACE, SERIES 5.

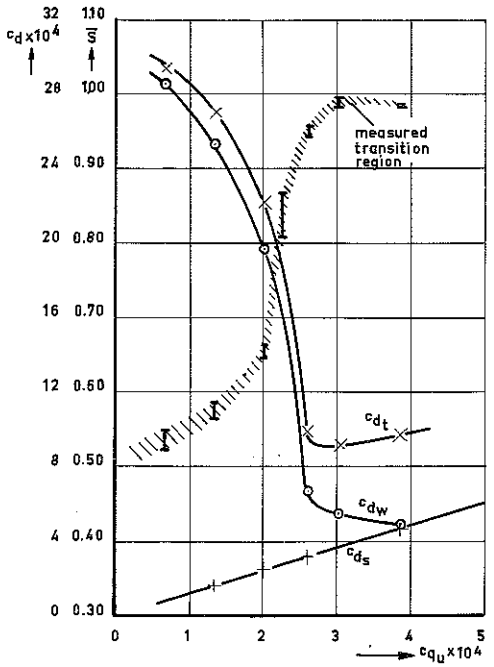

FIG.11.49: TRANSITION AND DRAG FOR THE UPPER SURFACE, SERIES 6.

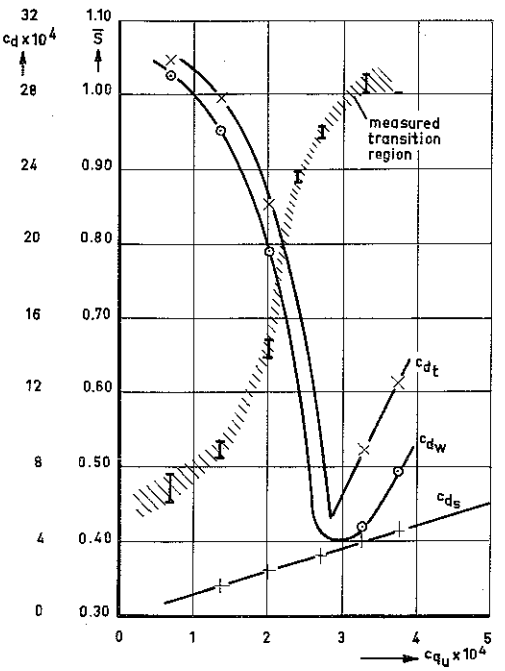

FIG.11.50: TRANSITION AND DRAG FOR THE UPPER SURFACE, SERIES 7.

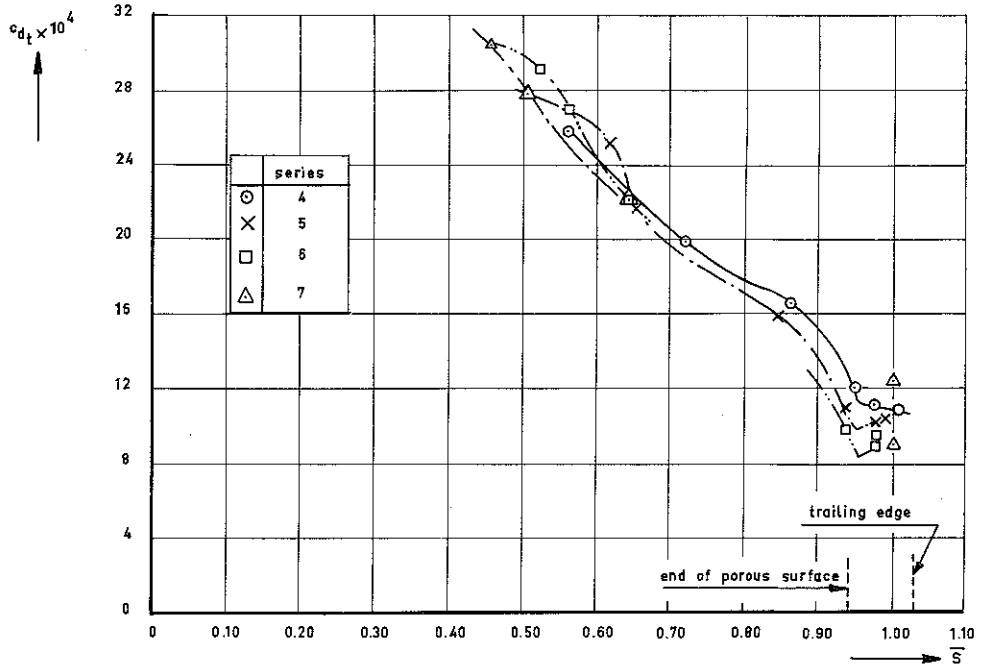

FIG.11.51: RELATION BETWEEN TOTAL DRAG AND POSITION OF THE BEGINNING OF TRANSITION FOR THE UPPER SURFACE ; SERIES 4–7.

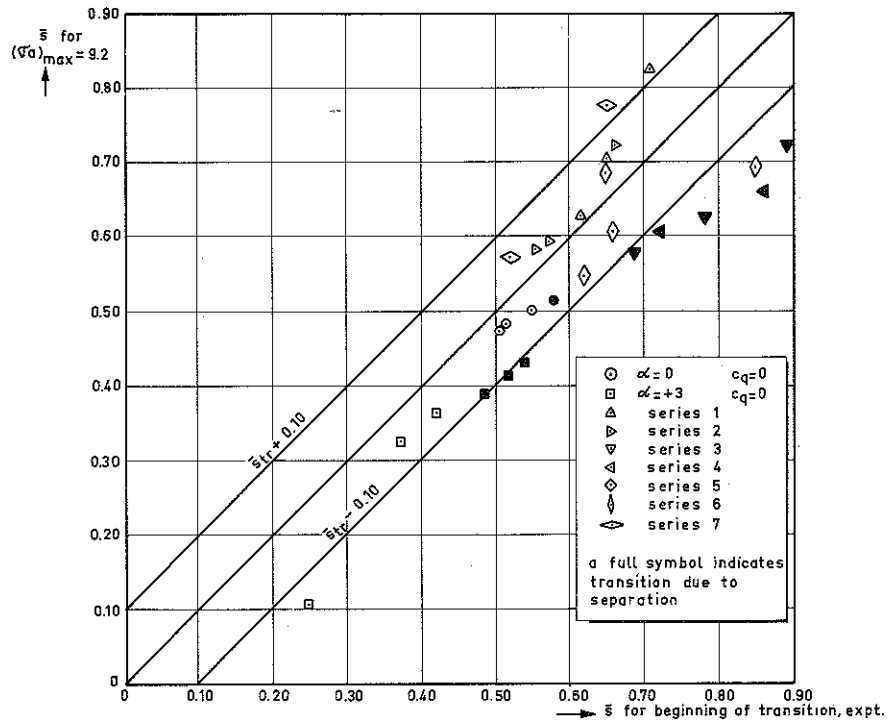

FIG. 11.52: SUMMARY OF MEASURED AND CALCULATED TRANSITION POSITIONS.

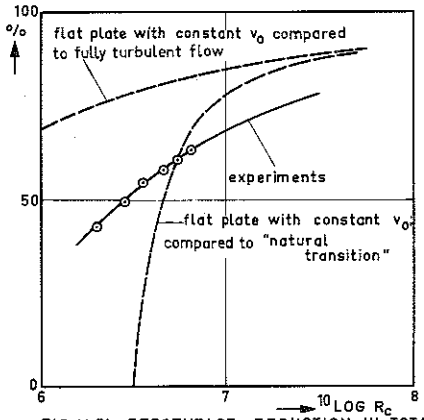

FIG. 11.54 : PERCENTAGE REDUCTION IN TOTAL DRAG FOR THE UPPER SURFACE OF THE SUCTION MODEL.

NOTE : FIG. 11.53: ON NEXT PAGE.

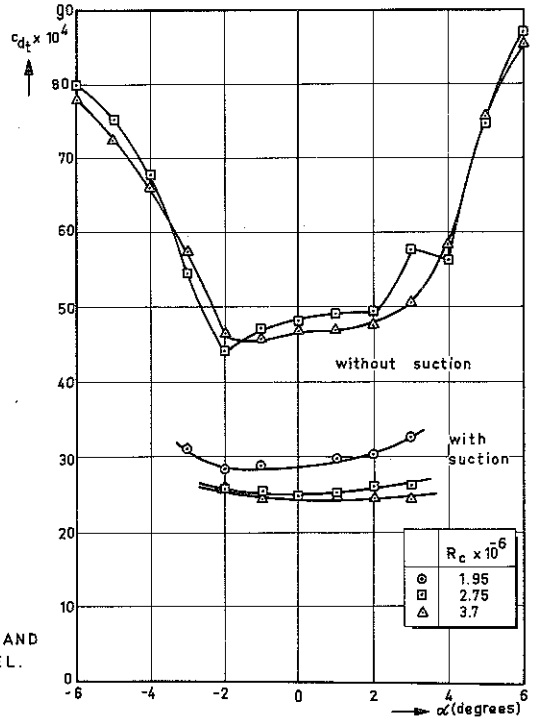

FIG. 11.55 : TOTAL DRAG FOR THE UPPER AND LOWER SURFACE OF THE SUCTION MODEL.

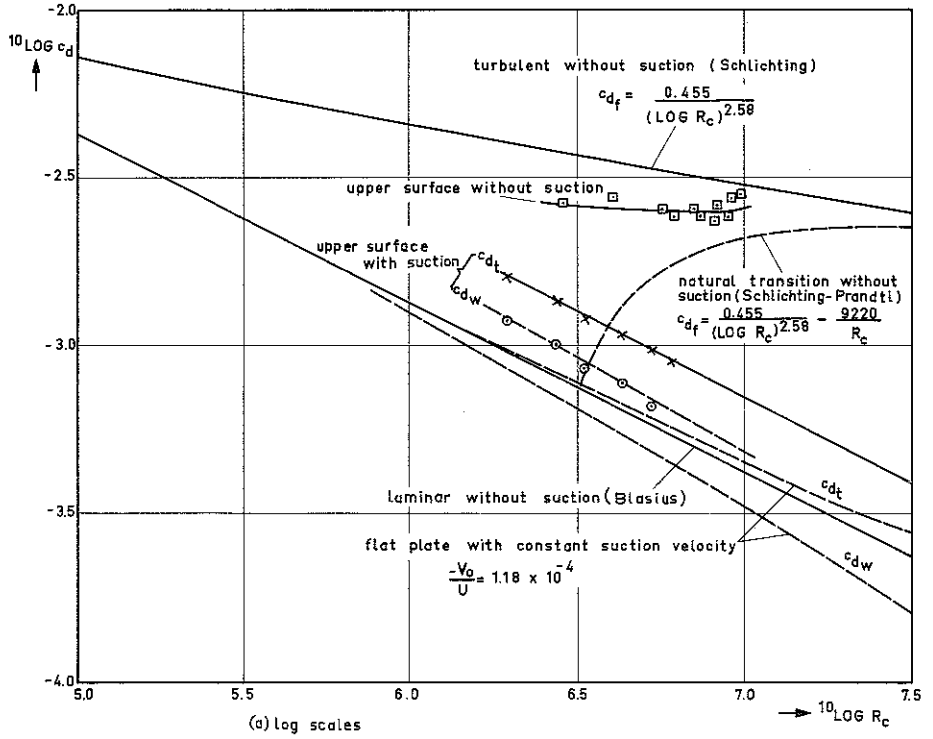

(a) log scales

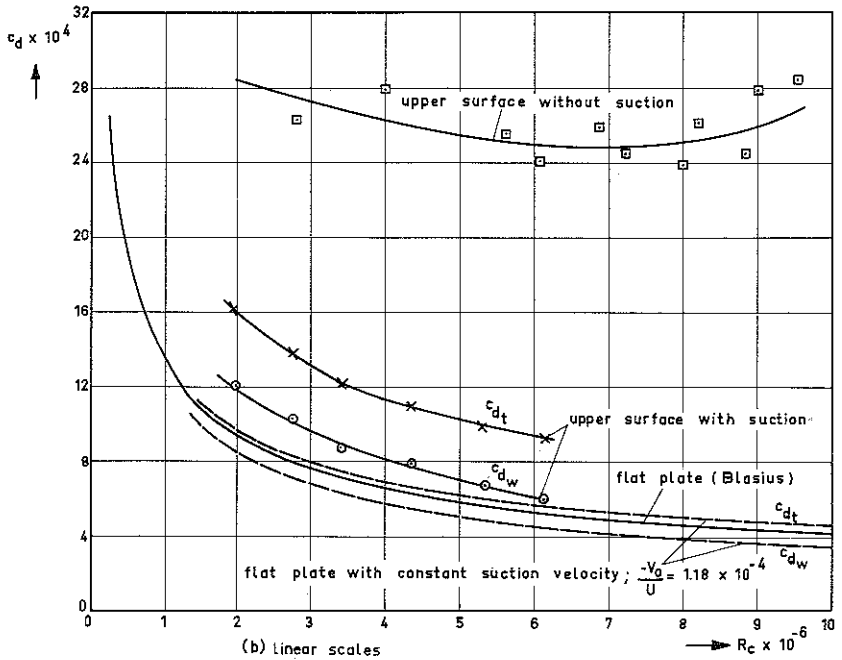

(b) linear scales

FIG. 11.53 : DRAG OF THE UPPER SURFACE COVERED WITH NYLON; VALVE SETTINGS OBTAINED BY TRIAL AND ERROR.